

Article

Impact of ICME- and SIR/CIR-Driven Geomagnetic Storms on the Ionosphere over Hungary

Kitti Alexandra Berényi ^{1,2,3,*} , Andrea Opitz ⁴, Zsuzsanna Dálya ⁴, Árpád Kis ³ and Veronika Barta ³ ¹ ELKH-ELTE Space Research Group, H-1117 Budapest, Hungary² Doctoral School of Environmental Sciences, ELTE Eötvös Loránd University, H-1117 Budapest, Hungary³ Institute of Earth Physics and Space Science, H-9400 Sopron, Hungary⁴ Wigner Research Centre for Physics, H-1121 Budapest, Hungary

* Correspondence: berenyi.kitti@epss.hu

Abstract: We investigate the differences between the effects of geomagnetic storms due to Interplanetary Coronal Mass Ejections (ICME) and due to Stream Interaction Regions or Corotating Interaction Regions (SIR/CIR) on the ionospheric F2-layer during the maximum of solar cycle 24. We have created a unique list of the ICME- and SIR/CIR-driven geomagnetic storm events for the time interval between November 2012 and October 2014. Finally, 42 clear ICME and 34 clear SIR/CIR events were selected for this analysis. The individual geomagnetic storm periods were grouped by seasons, time of day, and local time of Dst_{min} and were analyzed using three different methods: linear correlation analysis using 4-h averages of foF2 parameters and the geomagnetic indices (1st), daily variation of deltafoF2 (2nd), and 3D plotting: geomagnetic indices vs. time vs. deltafoF2 (3rd). The main phase day of the ICME- and SIR/CIR-induced geomagnetic storms was our main focus. We used manually evaluated ionospheric foF2 parameters measured at the Sopron ionosonde station and the geomagnetic indices (Kp, Dst, and AE) for this analysis. We have found that in most cases, the variation of the Dst index is the best indicator of the impact caused in the F2 layer. We conclude as well that the representation of the data by the third method gives a better description of the ICME and SIR/CIR-triggered storm behavior. In addition, our investigation shows that the SIR/CIR-related perturbations can be predicted with greater accuracy with the second method.

Keywords: ionosphere; ionospheric storms; geomagnetic storms; geomagnetic indices; space weather; solar eruptions; ICME-induced events; SIR/CIR-induced events



Citation: Berényi, K.A.; Opitz, A.; Dálya, Z.; Kis, Á.; Barta, V. Impact of ICME- and SIR/CIR-Driven Geomagnetic Storms on the Ionosphere over Hungary. *Atmosphere* **2023**, *14*, 1377. <https://doi.org/10.3390/atmos14091377>

Academic Editors: Emilia Correia, Jean-Pierre Raulin, Paulo Roberto Fagundes and José-Valentin Bageston

Received: 14 July 2023

Revised: 20 August 2023

Accepted: 27 August 2023

Published: 31 August 2023



Copyright: © 2023 by the authors. Licensee MDPI, Basel, Switzerland. This article is an open access article distributed under the terms and conditions of the Creative Commons Attribution (CC BY) license (<https://creativecommons.org/licenses/by/4.0/>).

1. Introduction

The most significant and well-documented effects in the ionosphere are those that occur during periods of global geomagnetic storms [1]. Previous studies have found two kinds of geoeffective heliospheric structures that can induce global geomagnetic storms [2–7]: 1. Interplanetary Coronal Mass Ejections (ICME-induced events); and 2. Stream Interaction Regions (SIRs)/Corotating Interaction Regions (CIRs). Many studies dealt with the identification and geoeffectiveness of these two types of geomagnetic storms [6,8–12].

In certain cases, there are persistent SIRs, which are by definition corotating but may or may not have completed one solar rotation. Allen et al. [13] employed the terminology SIR/CIR for them. Earlier studies have found that SIRs alone can trigger geomagnetic storms (e.g., [14–16]), affect the ionosphere/thermosphere at Earth (e.g., [5,17]), and be the major source of energetic particles in the interplanetary medium (e.g., [15,18]). When the source of the SIR corotates once around the Sun, then it is referred to as the corotating interaction region (CIR) [13].

When an ICME hits the magnetosphere, a rapid increase can be registered in the horizontal component of the magnetic field at ground-based magnetometers at equatorial and low latitudes, which is generally called Sudden Storm Commencement (SSC). This

initial phase of the geomagnetic storm is followed by the main phase, and then the recovery phase can last for several days. These storms are called SSC events or ICME-induced storm events. As previous studies determined, ICME-driven storms are primarily responsible for the major geomagnetic storms ($Dst_{\min} < -100$ nT) and for inducing higher levels of radiation belt electron flux [6,19]. In addition, the strength of the magnetospheric convection electric field of an ICME storm is often stronger than that of SIR/CIR storms [12]. We expect the most effective SSC (ICME-induced) events during the solar cycle maximum and more often than during the minimum.

The SIR/CIR-driven geomagnetic storms usually do not have an SSC phase, but the magnitude of the generated effects sometimes can be larger than the ICME-caused ones [3,5]. This is the result of the fact that a SIR/CIR storm has a longer duration and, therefore, can deposit roughly the same amount or even more energy into the upper atmosphere than most of the moderate ICME storms do over the entire period of their course [20,21]. The effects of SIR/CIR storms lead to elevated levels of spacecraft charging at GEO orbit for a longer duration and heat the nightside plasma sheet to a greater extent and for a longer duration [12,13]. These storms are also similar to ICME-induced events in their ability to generate electromagnetic ion cyclotron waves in the inner magnetosphere [22], which are an important loss mechanism for radiation belt electrons. These storms can be called Gradual Storm Commencement (GSC) events [1,23] or SIR/CIR storm events [11]. The intensity of these geomagnetic storms is typically weak to moderate, which is connected to the highly oscillatory nature of the GSM magnetic field z component within CIRs [3]. Generally, these GSC events are more typical during the solar cycle minimum [3,11], when there are fewer ICME events and hence fewer SSC events. It is important to mention that SIR/CIR and ICME-induced events can interact and be more geoeffective together than in isolated circumstances (e.g., [16]). The most geoeffective features are formed through the merging of two ICME-induced events [24].

Several definitions exist to determine a geomagnetic storm and its magnitude. Previous studies have typically identified and characterized storm events considering the magnitude of geomagnetic indices such as K_p or Dst [25]. In addition to these two indices, we used the AE-index, which measures the activity of the Auroral electrojet (in nT), so we can examine with this index whether the registered ionospheric perturbations come from the auroral region or not. The K_p -index represents the geomagnetic activity of the midlatitude regions, and its scale is logarithmic [26]. The Dst -index is the index of the equatorial ring current (in nT), thus it represents the geomagnetic activity effects coming from the equatorial region [27,28]. Using geomagnetic indices for describing ionospheric behavior during a geomagnetic storm is a rather complicated task [29]; see papers [30,31].

Geomagnetic storms generate so-called ionospheric storms in the ionosphere, which have similar evolution and phases as the geomagnetic storms themselves but with a faster course. The general course of the midlatitude ionospheric F2-layer response to geomagnetic storms was described by Rishbeth et al. [32] and recently summarized by Prölss [33] (see also reviews and case studies of [34–41]). As we mentioned above, the ICME and SIR/CIR-induced geomagnetic storms have different time courses and result in different magnitudes of ionospheric perturbations. Several processes have to be taken into consideration during the examination of the mid- and low-latitude ionosphere, namely: photo-production, chemical loss and transport by thermal expansion, neutral winds, waves, tides, and electric fields of internal and external origin [23]. To examine the response of the ionosphere during geomagnetic storms, several influential factors have to be considered, such as the magnitude of the geomagnetic activity, type of the geomagnetic storm, local time (LT) of the sudden storm commencement (SSC), times of the day (noon/dawn), season (winter/summer), and geomagnetic latitude [1,23,42].

There have already been studies that dealt with the correlation problem of geomagnetic indices and ionospheric parameters and also with foF2 forecasting during geomagnetic storms [43–50]. Linear regression methods are useful for studying the relationship between predictor and response variables; therefore, many studies have used them in the past to

model the ionospheric response as a function of solar and geomagnetic activity [51–57]. However, there is still not enough available research about the ionospheric electron density variability during different types of geomagnetic storms as a function of geomagnetic indices; therefore, we find it important to add more new results and knowledge to this field.

In this study, we take into account all the influential factors mentioned above. With our analysis, we search for correlation(s) between the magnitude of the two geomagnetic storm types (described here with the AE, Kp, and Dst indices) and the variation of the F2-layer maximum electron density (described with ionospheric foF2 parameter). This study helps to find out the relations among these parameters, which can be built into empirical space weather models (such as [58]). It is important to find the best input parameters for such models to predict the space weather effects more accurately. This study applies three methods to analyze the selected storm events: linear correlation analysis using 4-h averages of foF2 parameters and the geomagnetic indices (1st), daily variation of deltafoF2 (2nd), and 3D plotting of geomagnetic indices versus time versus deltafoF2 (3rd).

In the next section, we are going to describe the data, the catalogs, and the methods that were the basis of our storm event analysis. In the Result session, we show the plots created by the three different methods. Then in the Discussion and concluding remarks, we put the results into a complex view and compare them with previous studies.

2. Data and Methods

To perform the study, we created a unique database of clear geomagnetic storms generated by only SIR/CIR events that were separated from ICME-induced events in the November 2012–October 2014 time interval (the maximum of solar cycle 24, see [59]). Finally, 42 clear ICME and 34 clear SIR/CIR events were selected, which were listed in Tables S1 and S2 (see Supplementary Material). To determine the function between the geomagnetic storm magnitude and the variation of the foF2 parameter, three global geomagnetic activity indices were used: the Kp, Dst, and AE indices. As a first approach, we investigate the main phase of the geomagnetic storm, in other words, the Dst_{min} day (24 h in total).

2.1. Data

The following data were used to create the databases (for website links, see the Data Availability Statement section below):

1. SC (Sudden Commencement) times and the international quiet days (Q-days) from the Kp index are derived by GFZ Potsdam, Germany, and by ISGI (International Service of Geomagnetic Indices), Spain.
2. ICME source dates and ICME comments were used from different NASA websites.
3. ACE/WIND shock dates were provided by three different websites. In addition, we used the list of our co-authors, called Dalya & Opitz ACE ICME start and end dates (available on [60]).
4. CIR and solar wind high-speed stream (HSS) catalogs were also used for the creation of our list.
5. Solar and geomagnetic indices: The Dst-, AE- index, and Dst_{min} times were used with a 1-h resolution from OMNIWeb.
6. Ionosonde data: the ionospheric foF2 parameter data was taken from the ionosonde station of Nagycenk Geophysical Observatory, Hungary (IAGA code: NCK) [61]. Its McIlwain number is $L = 1.9$, geomagnetic latitude: 46.17° , geomagnetic longitude: 98.85° , and inclination (dip angle): 66.83° , therefore, this station is at a sub-auroral (midlatitude) site in the Northern Hemisphere. The parameters from the ionograms were evaluated manually. At the examined location, a Polish VISRC-2 type of ionosonde monitored the ionosphere between 2007 and 2018 [61–63]. The frequency range of the instrument was set to 1 MHz–16 MHz, and this range was divided into 1000 different frequencies during sounding. The instrument sampled

the ionosphere every half hour. The transmitter power was 500 W. With the manual ionogram processing software (called *ipp_ox*, developed by the Space Research Center of the Polish Academy of Sciences), the accuracy of the parameter readings is 1 km for altitude values and 0.05 MHz for frequencies (no automatically evaluated data are available).

2.2. Methods

The storm event should be individual, not starting during a previous one's recovery phase, and at least 24 h should be between the start times of the two events. This was defined based on the Dst index. The selected pure events were validated and checked using several storm event and satellite data catalogs, see above in the Data section. To consider all the mentioned influential factors, we separated the events into the following groups: season (summer, winter, or equinox), phase of the day, and type of the geomagnetic storm (ICME-induced or SIR/CIR-induced).

The selected pure events were analyzed by three types of methods:

1. The first (1st) method: Daytime changes of ICME and SIR/CIR events

After the categorization of Mendillo and Narvaez [23], the following phases of the day groups were analyzed: Midnight, Dawn, Morning, Noon, Afternoon/Dusk, and Night. These groups are represented in Figures 1–6 as 4-h averages of ionospheric foF2 parameters and the geomagnetic indices.

Time resolution: 4 h.

To get the relationship between the geomagnetic indices and the ionospheric foF2 parameter, we used linear regression on our data. The daytime intervals are: for the Dawn group 02–06:00 (UT), for the Morning group 06–10:00 (UT) the Noon group 10–14:00 (UT), Afternoon/Dusk group time interval is 14–18:00 (UT), for the Night group 18–22:00 (UT) and the Midnight group 22–02:00 (UT) (after [23]).

The 4-h mean values and the related standard deviations, along with the linear fitting results with the computed correlation coefficient (R) and the root-mean-square deviation (RMSD) are listed in Tables S4–S6 (Supplementary Material).

2. The second (2nd) method: Changes according to the local time of Dst_{min}

To get the real storm-time foF2 changes (the $\Delta foF2 = \Delta foF2$) in percentage, we used Equation (1), which is accepted and generally used also by other authors [11,63,64]:

$$\Delta foF2 = \left(\frac{foF2_{storm} - foF2_{quiet}}{foF2_{quiet}} \right) * 100\% \quad (1)$$

This equation for $\Delta foF2$ gives the relative foF2 parameter deviation from the median value of three quiet days. When the value in Figures 7–10 is 0%, the storm time value is equal to the median quiet day value at the respective half hour. In Table S3 we listed the used quiet days (Supplementary Material).

In addition to the above-detailed study groups, three new study groups were formed based on the local time of Dst_{min} point (see Table S7 in the Supplementary Material):

- Post-midnight: after midnight and before sunrise
- Daytime: after sunrise and before sunset
- Pre-midnight: after sunset and before midnight

Note that the sunset and sunrise times were individually and manually determined using ionograms.

Time resolution (equal to the time resolution of the ionosonde): 0.5 h.

3. The third (3rd) method: 3D plotting of geomagnetic indices versus time versus $\Delta foF2$

To visualize the geomagnetic index variations, we display the parameters in a 3D scatter plot. We add rainbow coloring according to the $\Delta foF2$ parameter changes in

harmony with the y-axis. Note that the Δf_oF_2 parameters were calculated during the second method. The same investigation groups were applied during the second method to separate the effects according to the seasons and the local time of the Dst_{min} .

Time resolution (equal to the time resolution of the geomagnetic indices): 1 h.

3. Results

Three methods were applied to analyze the selected 42 clear ICME- and 34 clear SIR/CIR-induced storm events. The main goal was to find characteristic similarities and/or differences between the ICME- and SIR/CIR-induced effects on the F2-layer electron density. Another goal was to find the geomagnetic index, which correlates best with the ionospheric F2-layer's electron density (f_oF_2 parameter) change during geomagnetic disturbances.

3.1. 1st Method: Daytime Changes of ICME and SIR/CIR Events

The selected events were grouped by season. For ICME-induced events, we have found 16 winter, 13 summer, and 13 equinox events. For SIR/CIRs, we have found 6 winter, 17 summer, and 11 equinox events. Results from the first method applied to these events are shown in Figures 1–6. Every data point represents a 4-h average of the geomagnetic indices and the f_oF_2 parameter (see the 4-h means with their standard deviations in Table S6 in the Supplementary Material). In Figures 1–6, we have separated the values on each plot according to the six phases of the day groups: Midnight, Dawn, Morning, Noon, Afternoon/Dawn, and Night.

Our aim was to determine a f_oF_2 trend as a function of the different geomagnetic indices. Therefore, we used linear regression on our data, marked with a red line in Figures 2, 4 and 6. We have also computed the related correlation coefficient[®] values and the root-mean-square deviation (RMSD), which indicate how accurate the linear fit to the data is (presented on the bottom left side of each plot in Figures 2, 4 and 6). The table with the basic linear fitting results along with the related correlation coefficient (R) and RMSD values can be found in Tables S4 and S5. Correlation coefficient (R) values greater than 0.5 are highlighted in the following sections. Note that for the Dst index, the correlation coefficient is opposing due to its naturally negative values; namely, the more negative value detected for Dst the larger the geomagnetic storm is.

3.1.1. Winter Events

In Figure 1a–c the 16 winter ICME events are plotted. The f_oF_2 values were obtained in the 2–12 MHz frequency range. In Figure 1d–f the 6 winter SIR/CIR events are plotted. The frequency range is the same as for the winter ICME-induced events. The positive ionospheric storm effect has the same magnitude during the daytime as the ICME events. Generally, we expect a more probably positive ionospheric storm phase in winter in the Northern Hemisphere at midlatitude. As a consequence of the fact that the background thermospheric wind circulation in winter is in the opposite direction to the storm-induced winds that move the negative phase from the pole to the equator, thus limiting the negative electron density region to higher latitudes during geomagnetic storms [29,34]. There are much fewer SIR/CIR events happening in winter in the Northern Hemisphere than ICME-induced events and the magnitude of the events is weaker. This agrees with the assumptions of the previous studies [5,11,16].

The results of the linear fitting separately for every phase of the day group and the corresponding correlation coefficient (R) values are shown in Figure 2 for the winter events (see Tables S4 and S5 for the linear fitting result and the listed correlation coefficient (R) values). During winter ICME-induced Dawn, Morning, and Noon groups show a significant decrease as a function of the geomagnetic indices; in other words, with the increase in the indices, we see a decrease in the f_oF_2 parameter (Figure 2a,c,e). The corresponding R values are the best for the Dst- f_oF_2 correlation, with $R = 0.5932$ for Noon (note that for the Dst index, the correlation coefficient is opposing due to its generally negative values), but for Morning groups the best $R = -0.761$ correlation is with the AE- f_oF_2 parameters. However,

the RMSD values of 1.429 and 1.029, respectively, do not show a very good linear fitting accuracy on the data. On the contrary, the Afternoon/Dusk, Night, and Midnight groups show an increasing foF2 trend as a function of the indices (Figure 2g,i,k). The corresponding best correlation coefficient values are for AE-foF2 correlation, where R equals 0.5471 and 0.5789 as long as RMSD equals 1.349 and 0.782 in the Afternoon/Dusk and Night groups.

For the winter SIR/CIR-induced events, the trend is not as nice as for ICME-induced events. This may be because there were only 6 clear events this season. The storm events of the Morning, Noon, and Afternoon/Dusk groups are the most unstable (Figure 2d,f,h). In the Dawn and Midnight groups, there is a decrease in foF2 as a function of the increasing storm magnitude (Figure 2b,l). However, during the night, a slight increase can be seen as a function of all three geomagnetic indices.

The most significant difference between the winter ICME- and SIR/CIR events is that there were much fewer SIR/CIR events during the winter. We assume that more than six events would be needed if we wanted to determine the trend in foF2 variability as a function of increasing storm magnitude. In addition, the changes in the ionospheric F-layer electron density during ICME-induced geomagnetic storm events are more stable and predictable than SIR/CIR-induced ones.

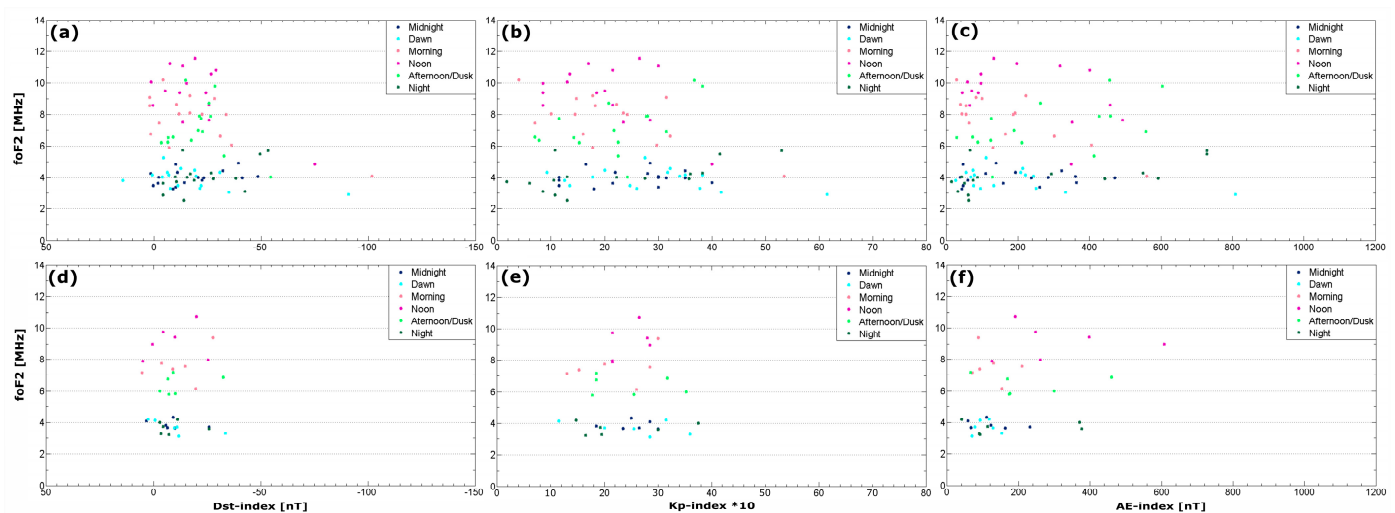


Figure 1. The 16 winter ICME 4-h average plots: (a) Dst index (nT), (b) Kp index*10, (c) AE index (nT) 4-h average values as a function of foF2 4-h average data. The 6 winter SIR/CIR plots: (d) Dst index (nT), (e) Kp index*10, (f) AE index (nT) 4-h average values as a function of foF2 4-h average data. The phase of the day groups are separated with different colors (see also the legend of the plots).

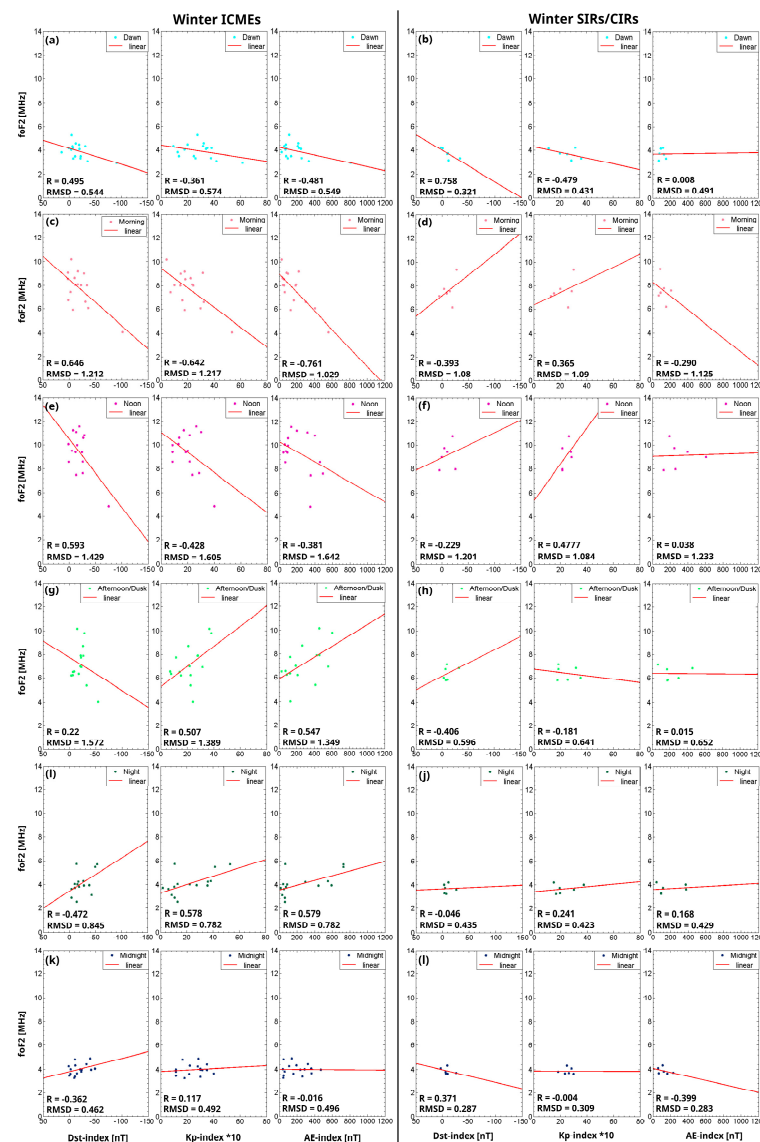


Figure 2. The linear fitting results of winter ICME-induced events phase of the day groups: (a) Dawn, (c) Morning, (e) Noon, (g) Afternoon/Dusk, (i) Night, (k) Midnight. The linear fitting results of the winter SIR/CIR phase of the day groups: (b) Dawn, (d) Morning, (f) Noon, (h) Afternoon/Dusk, (j) Night, (l) Midnight. Each phase of the day group portrays the foF2 parameters as a function of Dst, Kp, and AE indices too. The linear fitting line is with the red line. On the bottom left side of each plot, the correlation coefficient (R) and RMSD values are presented (see in the Supplementary Material Table S6 for 4-h mean values and see Tables S4 and S5 for the linear fitting results, R and RMSD values).

3.1.2. Summer Events

In Figure 3a–c the 13 summer ICME events are plotted. The foF2 values were obtained in the 4–10 MHz frequency range. In Figure 3d–f, the analysis results of the 17 summer SIR/CIR events are plotted. The foF2 frequency range is the same as the summer ICME-induced events. Compared with the winter storms, the frequency range is narrower and shows a descending trend as a function of the increasing storm magnitude (indices). Generally, we expect more frequent negative ionospheric storm phase at midlatitude in summer in the Northern Hemisphere because, in summer, the background thermospheric wind circulation coincides with the storm-induced one, allowing the negative storm phase to reach lower latitudes [29,34]. The type of the geomagnetic storm (ICME- or SIR/CIR-induced) does not affect this feature.

In Figure 4a–l, we show the phase of the day groups on individual plots along with the linear fitting with the corresponding R and RMSD values on the bottom left side of each plot (the summary of these data can be found in Tables S4 and S5). For the Dawn, Morning, Night, and Midnight groups, we see quite the same decreasing trend as a function of the geomagnetic indices for both ICME- and SIR/CIR-induced geomagnetic storms (Figure 4a–d,i–j). ICME-induced events do not show any significant trend in the Noon and Afternoon/Dusk (Figure 4e,g), which can also be seen from the R -values. On the contrary, the Noon and Afternoon/dusk groups of SIR/CIR events show a decreasing trend in foF2 with increasing storm intensity during the summer, similarly to the first three times of day groups. If we see the correlation coefficient values, it can be concluded that ICME-induced events are the best for Dst-foF2 correlation, with $R = 0.8095$ and 0.5631 , where $RMSD = 0.49$ and 0.476 for Night and Midnight groups (note that for Dst index the correlation coefficient is opposing due to its generally negative values). In addition, the best fitting is for Kp-foF2 correlation, with $R = -0.553$, where $RMSD = 0.882$ for the Morning group. As for SIR/CIRs, the best correlation coefficient (R) with $R = 0.7873$ value is connected to the Dst-foF2 correlation for the Night group, where $RMSD = 0.609$. In the other cases, the R values vary between -0.357 and -0.698 and none of the foF2 parameter and geomagnetic indices can be highlighted.

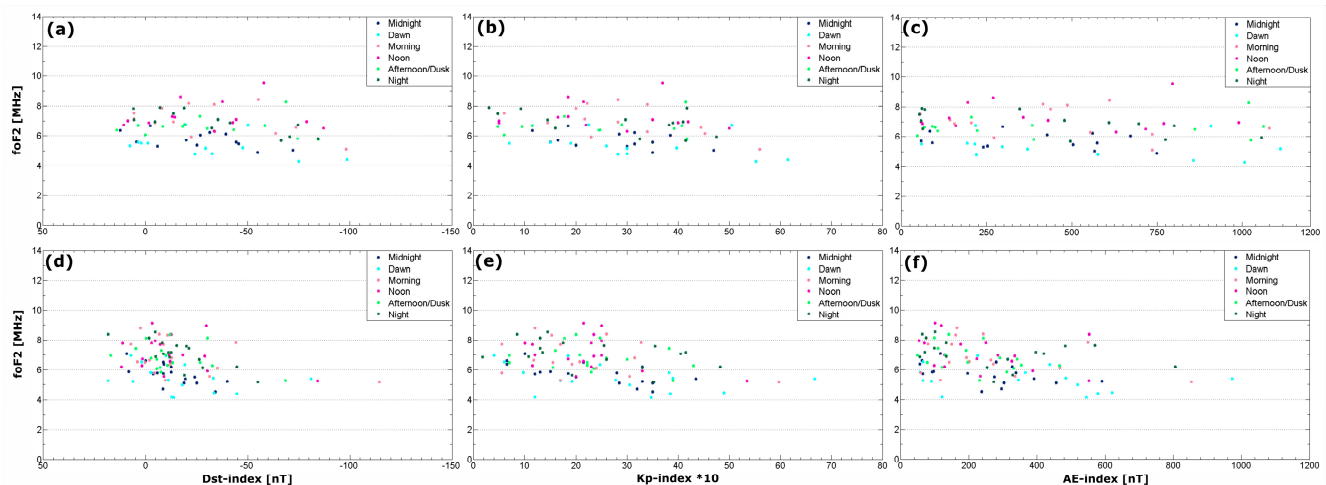


Figure 3. The 13 summer ICME plots: (a) Dst index (nT), (b) Kp index*10, (c) AE index (nT) 4-h average values as a function of foF2 4-h average data. The 17 summer SIR/CIR plots: (d) Dst index (nT), (e) Kp index*10, (f) AE index (nT) 4-h average values as a function of foF2 4-h average data. The phase of the day groups are separated with different colors.

Our results show that the ICME- and SIR/CIR-induced geomagnetic storm effects in the ionosphere are similar during the day in all six 4-h intervals. An exception to this is the results for the Noon and Afternoon/Dusk groups associated with ICME events, where no trend can be identified. It can therefore be concluded, in agreement with the results of previous studies, that as the geomagnetic indices increase, a negative ionospheric storm phase is most probable in summer in the Northern Hemisphere [29,34].

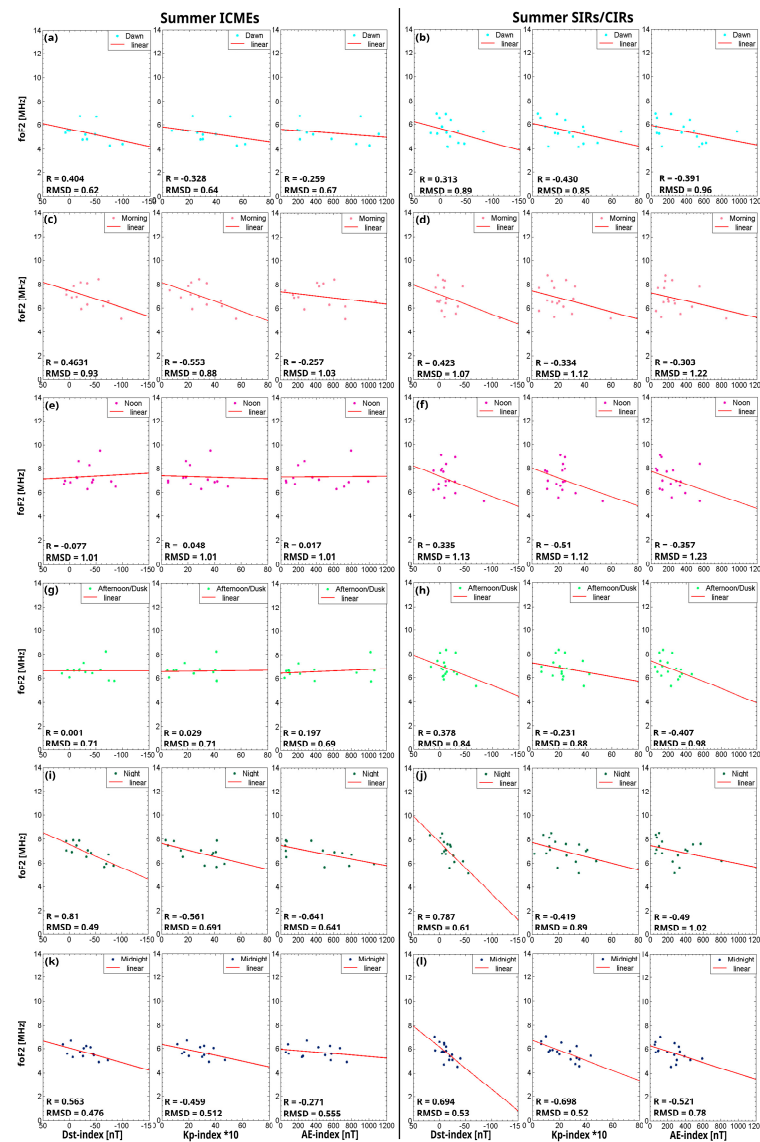


Figure 4. The linear fitting results of summer ICME-induced events phase of the day groups: (a) Dawn, (c) Morning, (e) Noon, (g) Afternoon/Dusk, (i) Night, (k) Midnight. The linear fitting results of the summer SIR/CIR phase of the day groups: (b) Dawn, (d) Morning, (f) Noon, (h) Afternoon/Dusk, (j) Night, (l) Midnight. Each phase of the day group portrays the foF2 parameters as a function of Dst, Kp, and AE indices too. The linear fitting line is with the red line. On the bottom left side of each plot, the correlation coefficient (R) and RMSD values are presented (Supplementary Material Table S6 for 4-h mean values and see Tables S4 and S5 for the linear fitting results, R, and RMSD values).

3.1.3. Equinox Events

In Figure 5a–c, the results of the 13 equinox ICME-induced events can be seen. The foF2 frequency range is between 3–11 MHz during the day. In Figure 5d–f, the 11 equinox SIR/CIR-induced events are plotted. The foF2 values were obtained in the 3–12.5 MHz frequency range. The dispersion of the data is larger for equinox events, and the data of the phase of day groups are also much more spread out by frequency and do not show a consistent picture compared to winter and summer data.

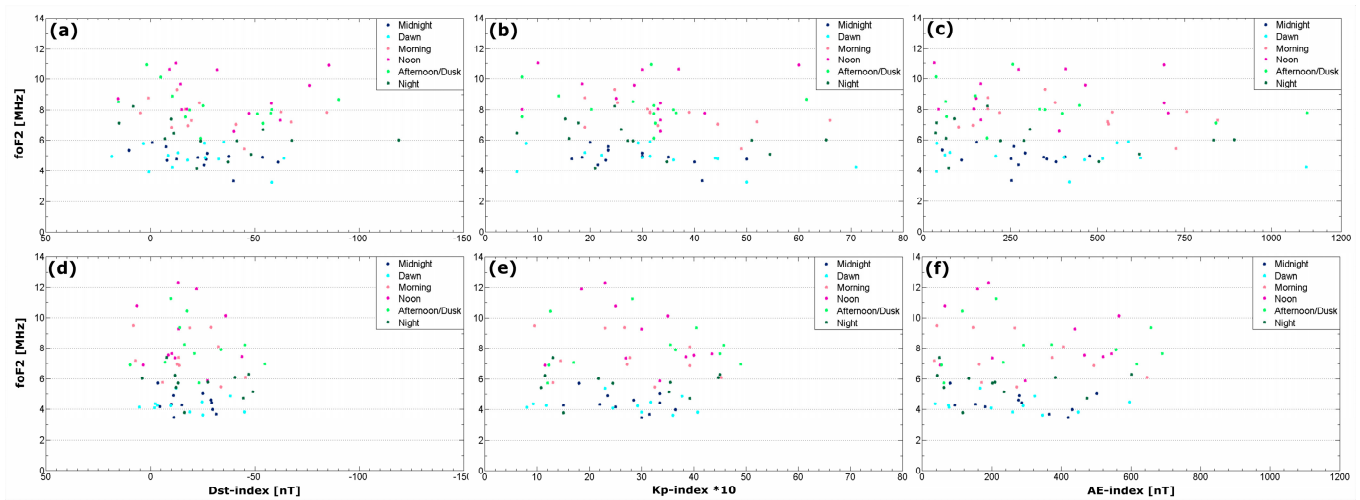


Figure 5. The 13 equinox ICME plots: (a) Dst index (nT), (b) Kp index*10, (c) AE index (nT) 4-h average values as a function of foF2 4-h average data. The 11 equinox SIR/CIR plots: (d) Dst index (nT), (e) Kp index*10, (f) AE index (nT) 4-h average values as a function of foF2 (MHz) 4-h average data. The phase of the day groups are separated with different colors.

In Figure 6, the phases of the day groups are portrayed separately along with the linear fitting with the corresponding R and RMSD values on the bottom left side of each plot. For Dawn, we do not see any significant trend in the data (Figure 6a,b). For Morning, Night, and Midnight we observe a significant decrease in electron density as a function of all geomagnetic indices. The Noon and Afternoon/Dusk group data are more scattered; therefore, the trends cannot be determined. In addition, the calculated correlation coefficient (R) values show that the variation of the foF2 parameter and the geomagnetic indices are not correlated during this season; the maximum R-value is 0.528, where RMSD = 0.879 for the Morning group of ICME events. However, this statement still needs to be verified. We propose a cross-correlation analysis of the data to determine whether there is a temporal difference between the processes responsible for the parameter changes.

The most significant difference between the ICME- and SIR/CIR-driven geomagnetic storms during equinox is that the foF2 frequency range of SIR/CIR events is wider and the magnitude of the events is more limited. The similarity is that according to the results, we expect mostly electron density to decrease (negative phase) during the day as the storm's magnitude increases.

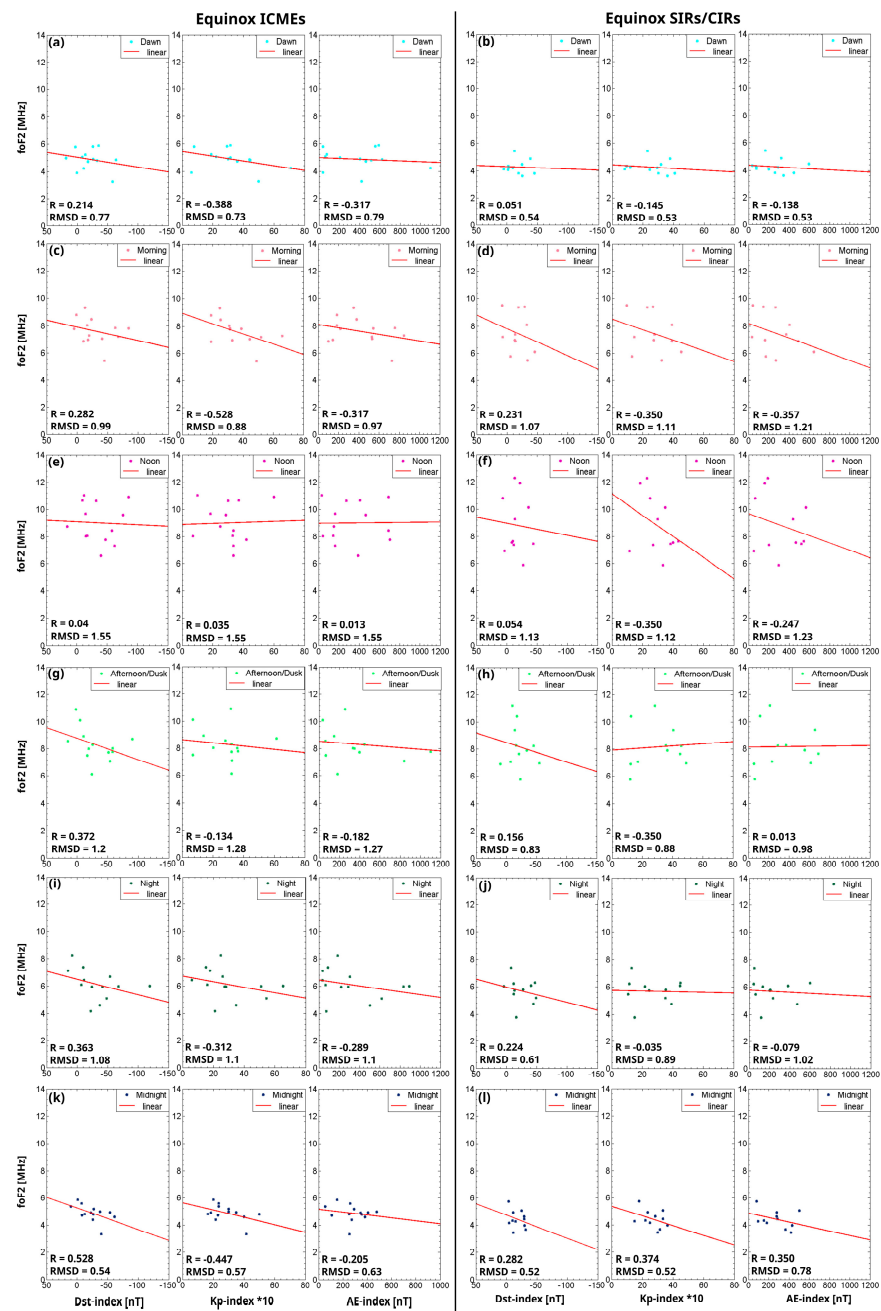


Figure 6. The linear fitting results of equinox ICME-induced events phase of the day groups: (a) Dawn, (c) Morning, (e) Noon, (g) Afternoon/Dusk, (i) Night, (k) Midnight. The linear fitting results of the winter SIR/CIR phase of the day groups: (b) Dawn, (d) Morning, (f) Noon, (h) Afternoon/Dusk, (j) Night, (l) Midnight. Each phase of the day group portrays the foF2 parameters as a function of Dst, Kp, and AE indices too. The linear fitting line is the red line. On the bottom left side of each plot, the correlation coefficient (R) and RMSD values are presented (see in the Supplementary Material Table S6 for 4-h mean values and see Tables S4 and S5 for the linear fitting results, R, and RMSD values).

3.2. Second Method: Changes According to the Local Time of the Dst_{min}

The $\Delta foF2$ (%) values are defined as the percentage foF2 parameter deviation from the median of the quiet day values. They were calculated according to Equation (1). The $\Delta foF2$ values as a function of time (UT) are shown in Figure 7. The events are investigated by seasons and separated by the Dst_{min} times as described previously (Section 2.2)

(see also Table S7). In Figure 7 and Figures S1–S3 (Supplementary Material), the results are portrayed.

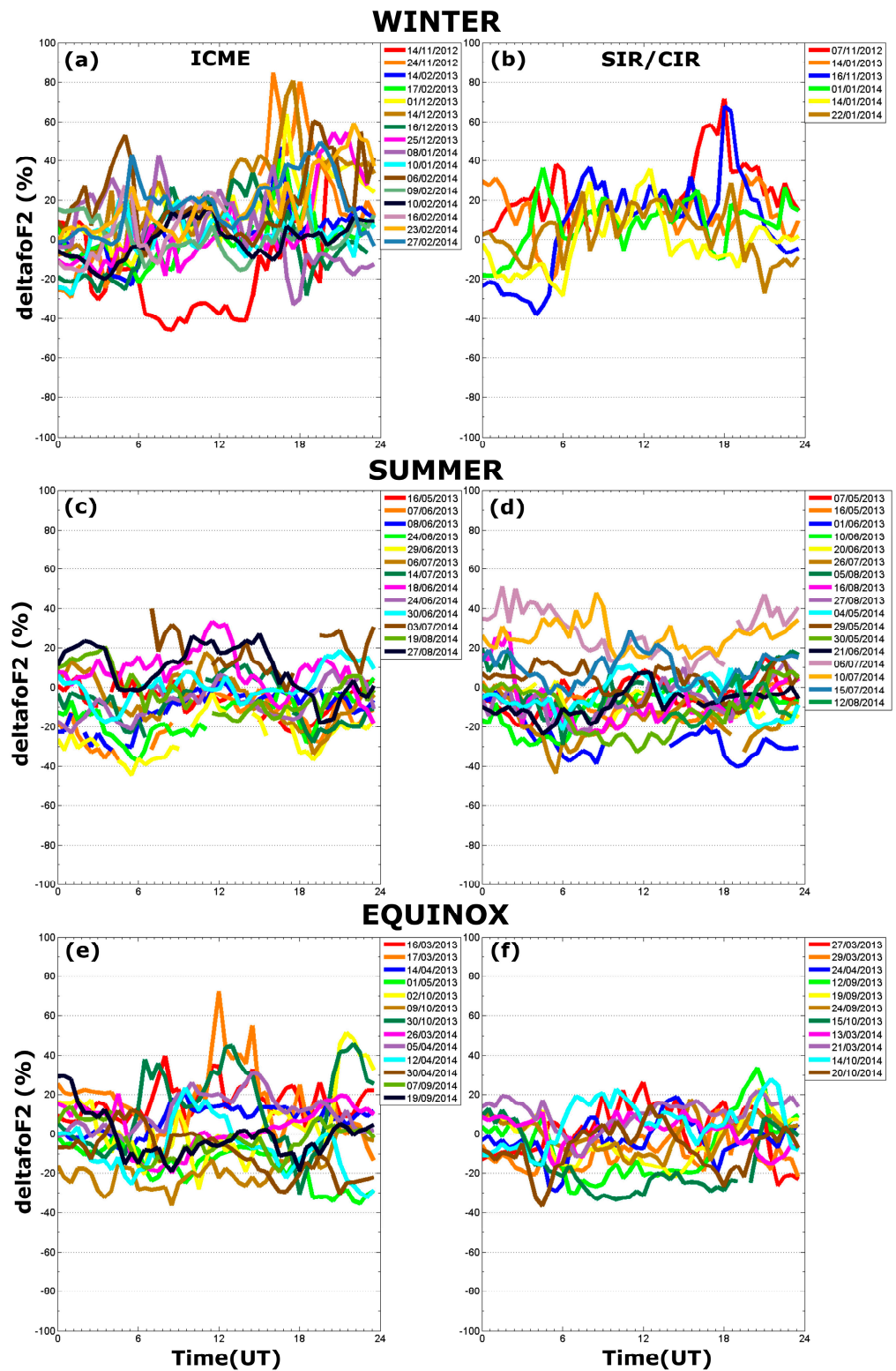


Figure 7. All season ICME vs SIR/CIR plots with the exact days in the legend panel: (a,b) winter, (c,d) summer, (e,f) equinox events are plotted, the deltafoF2 (%) values as a function of time (UT).

Figure 7 is a summary plot of the events during all seasons, and the individual events are with different colors, which indicates the exact storm. During winter, the deltafoF2 value

is between -46 – 85% for ICME-induced events and -38 – 71% for SIR/CIR-induced events (Figure 7a,b, Table 1). The deltafoF2 during the latest case seems to show a well-defined daily variation. During summer events, the deltafoF2 range is -44 – 40% for ICME-induced events and -43 – 51% for SIR/CIR-induced events (Figure 7c,d, Table 1). Here, a daily pattern of foF2 appears in the case of ICME-induced events. During equinox events, the deltafoF2 range is -36 – 72% for ICME-induced events and -37 – 34% for SIR/CIR-induced events (Figure 7e,f, Table 1), and no typical daily variation can be detected.

Table 1. The summary table of the deltafoF2 (%) value ranges for the three Dst_{min} time groups during all seasons and sorted for the two geomagnetic storm types (ICME- and SIR/CIR-induced events).

	deltafoF2(%) Value Ranges					
	WINTER		SUMMER		EQUINOX	
	ICME	SIR/CIR	ICME	SIR/CIR	ICME	SIR/CIR
post-midnight	-33% to 50%	-38% to 68%	-37% to 18%	-29% to 20%	-36% to 30%	-33% to 13%
daytime	-46% to 85%	-27% to 33%	-44% to 40%	-40% to 48%	-32% to 52%	-21% to 22%
pre-midnight	-22% to 81%	-18% to 71%	-37% to 33%	-43% to 51%	-36% to 72%	-37% to 34%
ALL	-46% to 85%	-38% to 71%	-44% to 40%	-43% to 51%	-36% to 72%	-37% to 34%

Generally, the most important features are as follows:

- (1) ICME can cause larger disturbances in the F2-layer electron density both in the negative and positive directions, while the impact caused by the SIR/CIR-driven storms is more moderate (especially during winter and equinox).
- (2) The effect in the second case (SIR/CIR-driven storm) has clearer seasonal dependence: one can see a positive phase in the winter, while a mainly negative phase occurs in summer during the day.
- (3) In winter, we can see the dusk effect (increased values after sunset) in both cases.

In order to get a clearer picture of the events, we separated the events by Dst_{min} time. According to the three study groups (post-midnight, daytime, and pre-midnight groups), the deltafoF2 values are shown in Figures S1–S3 and summarized in Table S7 in the Supplementary Material. The detailed analysis of the deltafoF2 parameters with the figures (Figures S1–S3) can be found in the Supplementary Material, Supplementary Results section. The Dst_{min} times are marked with colored dashed lines on those figures. A summary Table 1 is constructed with the deltafoF2 parameter ranges during the different seasons for all Dst_{min} time groups.

It can be concluded that such an analysis cannot determine an obvious trend in the deltafoF2 value, thus any typical storm-time ionospheric perturbations. The results suggest time delays in the effects caused, which can be nicely investigated with, e.g., cross-correlation or superposed epoch analysis methods. This needs further study.

3.3. Third Method: 3D Plotting of Geomagnetic Indices Versus Time Versus deltafoF2

In this part, the results of the third method are displayed and analyzed. In Figures 8–10, the deltafoF2 parameter as a function of time and the geomagnetic indices can be seen. Here we also applied the categorization of the events according to the Dst_{min} time. Using rainbow coloring of the deltafoF2 changes helps us to distinguish the positive (red) and negative (blue) deviations in the electron density during the geomagnetic storm events. For minimum and maximum values in deltafoF2; see Table 1 above. This method allows us to investigate the storm-time electron density anomalies in the F2 layer by viewing it in a more complex but clearer way.

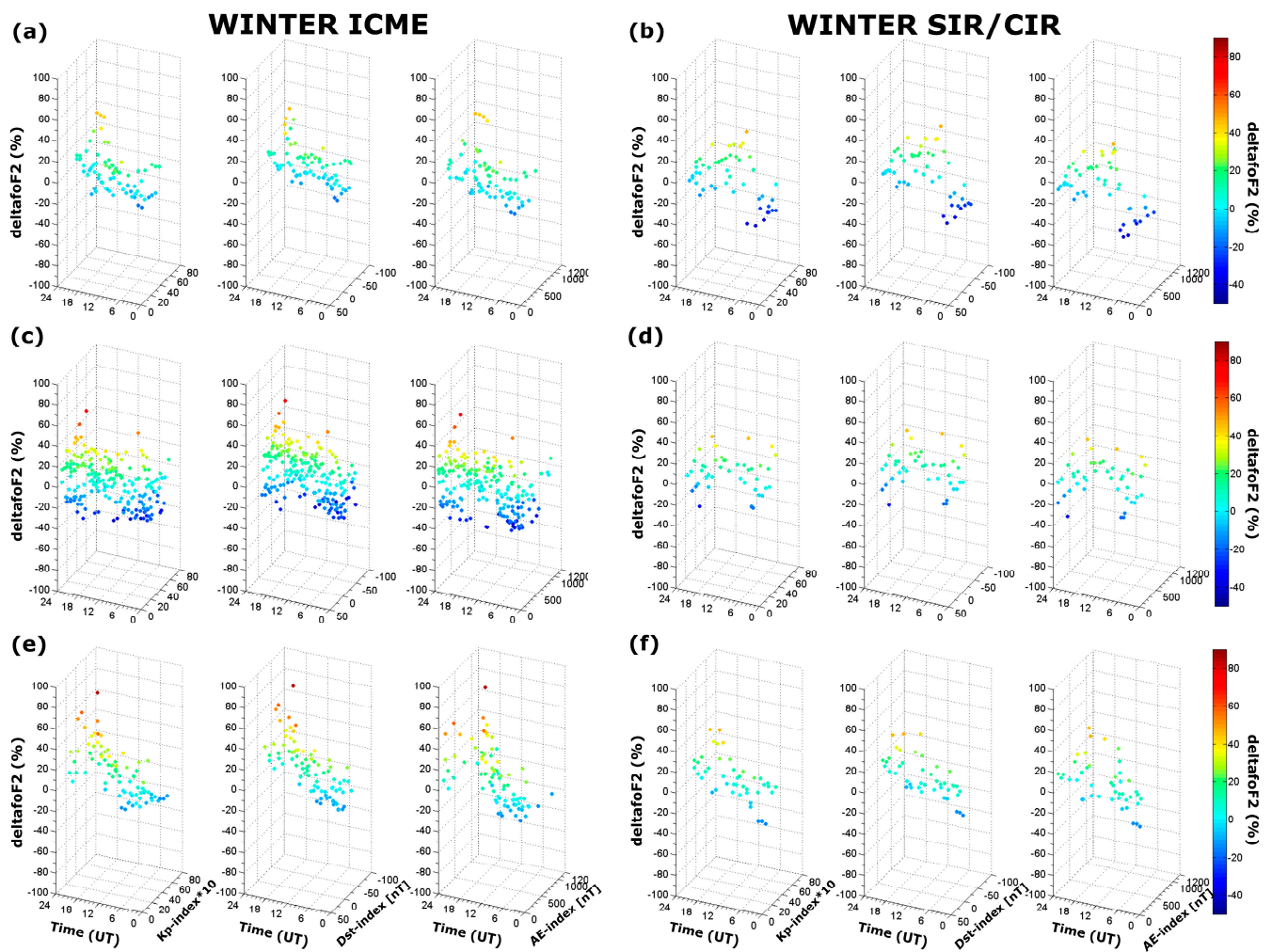


Figure 8. The winter ICME versus SIR/CIR 3D scatter plots: (a,b) post-midnight, (c,d) daytime, (e,f) pre-midnight deltafoF2 (%) values as a function of time (UT) and of geomagnetic indices (Kp, Dst and AE index). Rainbow coloring of the deltafoF2 changes mark nicely in the positive (red) and negative (blue) deviations in the electron density.

In Figure 8, the winter ICME and SIR/CIR events are plotted using the Dst_{min} time categorization (post-midnight, daytime, and pre-midnight). The post-midnight group in Figure 8a,b shows that the electron density increases slightly with increasing storm intensity due to ICME-induced events, with the maximum value of deltafoF2 peaking after sunset (Figure 8a). For SIR/CIR-induced events, the data show a deeper decrease after midnight until sunrise, followed by an increase in electron density as the magnitude of the storm increases, with a peak in deltafoF2 around noon (Figure 8b). The ICME-driven daytime groups show a more variable picture (Figure 8c). For the weaker storms, negative deltafoF2 values are seen at all hours. For the more intense geomagnetic storms, the electron density starts to decrease after midnight, then starts to increase and peaks at noon and after sunset, with a deltafoF2 value of $\sim 60\%$ for all geomagnetic indices. For SIR/CIR-driven events, we can see similar daytime storm strength-related changes; however, more cases than six are needed to get a clearer picture of this type of event (Figure 8d). The ICME events of the pre-midnight group show increasing deltafoF2 values during the day, reaching a maximum after sunset (dusk effect). The deltafoF2 reached its maximum value during the time of maximum geomagnetic activity, as indicated by the three indices (Figure 8e). The evolution of deltafoF2 caused by SIR/CIR events (Figure 8f) shows a similar picture but with smaller values.

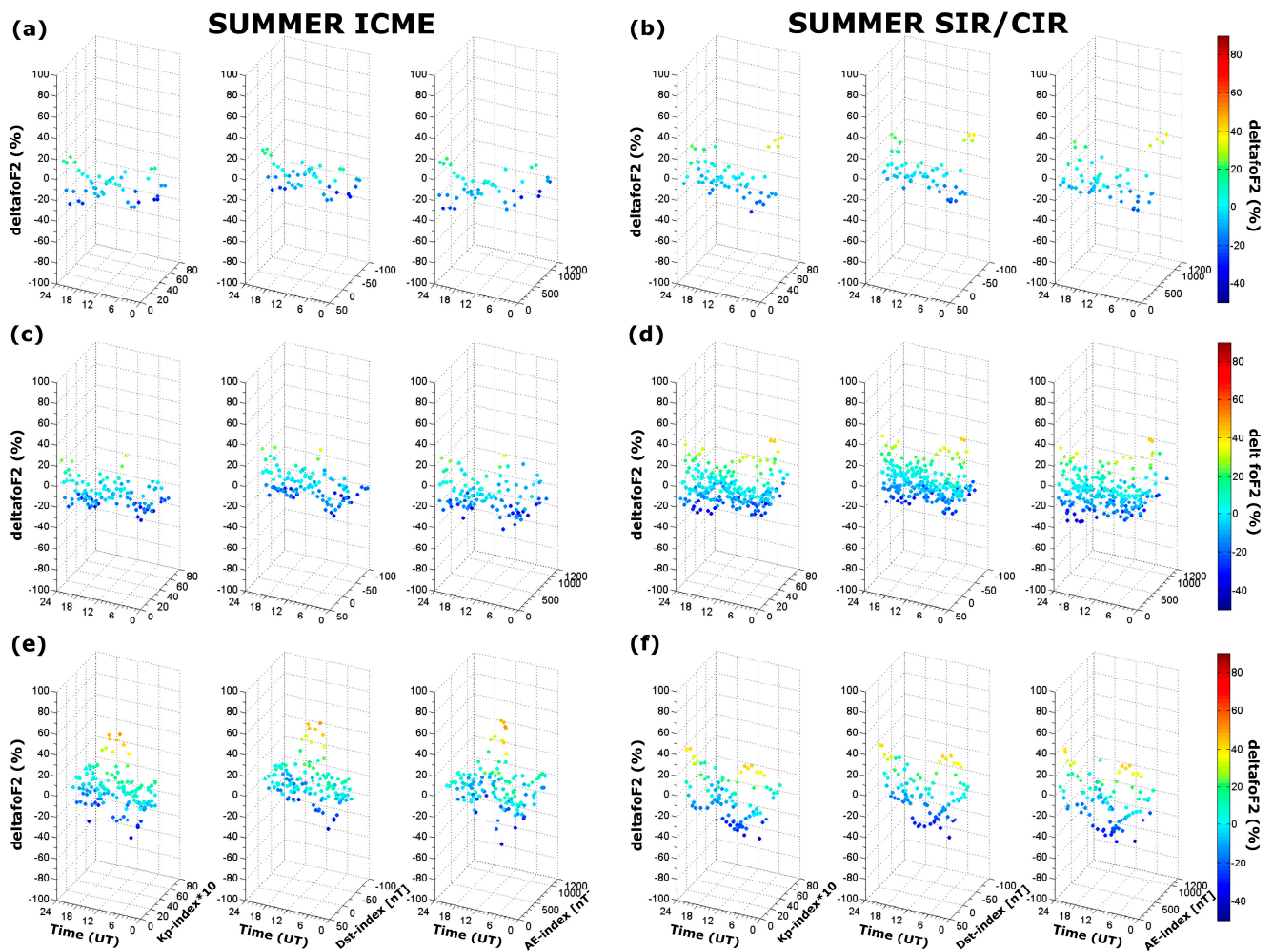


Figure 9. The summer ICME versus SIR/CIR 3D scatter plots: (a,b) post-midnight, (c,d) daytime, (e,f) pre-midnight deltafoF2 (%) values as a function of time (UT) and of geomagnetic indices (Kp, Dst and AE index). Rainbow coloring of the deltafoF2 changes mark nicely in the positive (red) and negative (blue) deviations in the electron density.

The results of summertime events using the third method are portrayed in Figure 9. The post-midnight group of the ICME-induced events in Figure 9a,b shows just a slight enhancement in deltafoF2 as a function of time and the geomagnetic activity around midnight, but mostly decreased values were observed; furthermore, we cannot detect any geomagnetic index dependency (Figure 9a). For SIR/CIR-related effects, we can see in the data that quite deep depletion in deltafoF2 is presented during low geomagnetic activity. The value increases up to ca. 35% around the sunrise hours, just for a short duration (Figure 9b). For the daytime group in Figure 9c, the deltafoF2 values vary between more limited ranges. Most deltafoF2 values show a significant decrease from its quiet day value before sunrise and after sunset. Two slightly increased deltafoF2 values (20–35%) are seen around noon and near midnight during the periods of the increased geomagnetic indices. On the contrary, SIR/CIR events show a clear trend, with the electron density increasing continuously throughout the day as geomagnetic activity increases (Figure 9d). One significant peak with 45% at 7–8 UT should be highlighted, which collocate with the maximum values in the geomagnetic indices. The ICME events of the pre-midnight group show also a continuous deltafoF2 increase as a function of geomagnetic indices; however, the maximum values (55%) are limited in time, between 12 and 18 UT (Figure 9e). The results of the SIR/CIR-driven events of this group are portrayed in Figure 9f. The deltafoF2 seems to also depend on geomagnetic activity; furthermore, it shows two peaks (45%)

from 10–17 UT and around midnight. Nevertheless, it can be concluded, according to our analysis, that most of the time one can expect negative ionospheric storms (decreased electron density) during the summer.

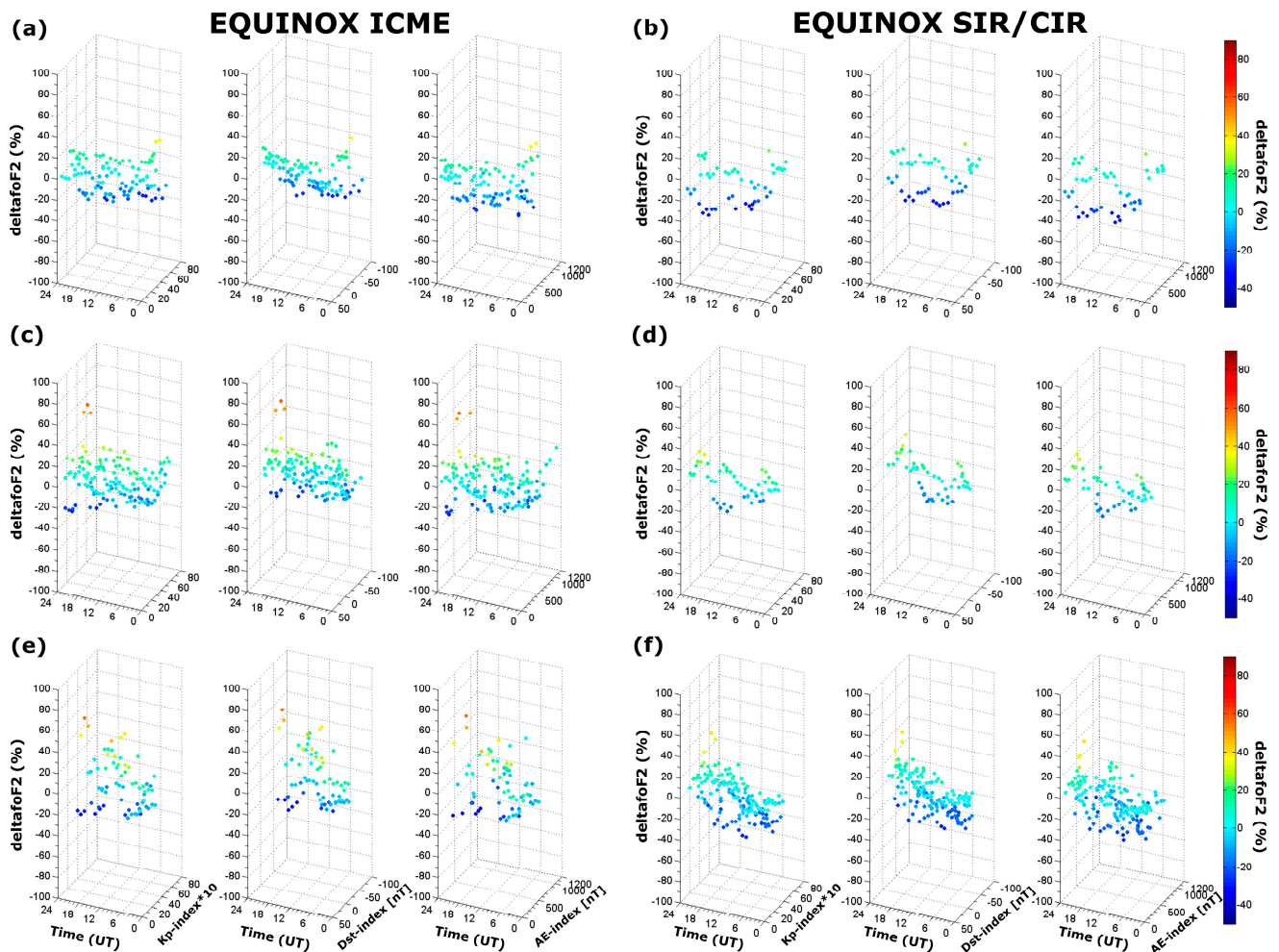


Figure 10. The equinox ICME versus SIR/CIR 3D scatter plots: (a,b) post-midnight, (c,d) daytime, (e,f) pre-midnight deltafoF2 (%) values as a function of time (UT) and of geomagnetic indices (Dst, Kp and AE index). Rainbow coloring of the deltafoF2 changes mark nicely the positive (red) and negative (blue) deviations in the electron density.

Figure 10 shows the results of the third method for equinox ICME- and SIR/CIR-driven events. As for the post-midnight group, we mostly see a decrease in electron density in our data; however, as shown in Figure 10a, an increased deltafoF2 (40%) is seen during the short period of 6–7 UT during the time of highest geomagnetic activity. For SIR/CIR events, we see mostly negative or no deviation during the whole day, and no significant positive peak in deltafoF2 can be observed (Figure 10b).

Investigating the data for the daytime group of ICME-induced events, we observe a decrease in electron density with a minimum deltafoF2 value of -32% , which then shows a steady increase with the increase in geomagnetic indices, peaking at 52% from sunset (from about 18UT). (Figure 10c). The SIR/CIR events of this group are more limited in deltafoF2, -21 – 22% , but the same increasing pattern is represented as a function of geomagnetic activity, peaking around midnight (Figure 10d).

The ICME events of the pre-midnight group show a significant negative deviation in deltafoF2 for the low geomagnetic index values from post-midnight to dawn hours (Figure 10e). Quite similarly to the daytime event evolution, the electron density increases with the increase in the geomagnetic indices and peaks (72%) around midnight. For

SIR/CIR events, the same evolution pattern can be seen, just with a more limited Δf_oF_2 range (Figure 10f).

4. Discussion and Concluding Remarks

During this study, 42 clear ICME and 34 clear SIR/CIR events were analyzed with three different methods, which are described in the Method section. The main phase days of the ICME- and SIR/CIR-induced geomagnetic storms are investigated during the maximum of solar cycle 24 (November 2012–October 2014). Our aim was to find similarities and differences between the ionospheric effects of ICME and SIR/CIR-driven storm events and to correlate the magnitude of the geomagnetic activity (K_p , AE, Dst index) and the caused ionospheric electron density variability (f_oF_2 parameter). This kind of comparative study of the ionospheric response to two different geomagnetic storms using statistical analysis is rather rare in the literature. Our motivation was also to fill this gap. In this section, a complex discussion of the above-detailed results of the three methods will be presented.

As a first approximation, we applied the phase of the day categorization of Mendillo and Narvaez [23] to our events (first method, see Section 3.1). Based on their method, we calculated the 4-h averages of the f_oF_2 parameter, and then these average values were correlated with geomagnetic indices during a 24-h time interval. Seasonal and diurnal variations, magnitude, and source type of the geomagnetic storms were considered during this analysis. The deviation from the median quiet day f_oF_2 values was calculated, named as Δf_oF_2 parameter (%) in the second and third methods. In both cases, the Δf_oF_2 parameter changes were investigated as a function of time, separated by seasons and local time of Dst_{\min} . The third method portrays the Δf_oF_2 changes as a function of time and geomagnetic indices in a 3D scatter plot. All three methods have their own advantages and disadvantages. One can determine quantitatively the observed changes using the first method: the strength of the relationship (R-value) between the f_oF_2 and the different geomagnetic indices (Dst, K_p , and AE) and the extent of the linear relationship between them (RMSD) can be quantified. In general, quite a low correlation has been found between the indices and the f_oF_2 changes. Nevertheless, the Dst index has a stronger correlation with the f_oF_2 change in most of the cases than the other two indices. Furthermore, the RMSD values are smaller usually in the case of the Dst index, too. Therefore, the linear relationship seems to be more adequate between the Dst and the f_oF_2 parameters comparing it with the other cases. The advantage of the second method is that in some cases the Δf_oF_2 shows a daily variation pattern, and the seasonal dependence of the effect caused by the two different types of storms can be recognized. Furthermore, although third is not able to quantify the changes, the dependence of f_oF_2 on storm intensity is quite clearly visible in the 3D plots. Therefore, it provides a better picture for determining the changes in electron density as a function of increasing geomagnetic activity and time. It also suggests that the time of the Dst_{\min} should always be taken into account, as different ionospheric responses can be expected depending on the time of day when the Dst_{\min} occurred or when the equatorial ring current was the strongest.

The similarities and differences between the ionospheric responses to the two types of geomagnetic storms (ICME or SIR/CIR) are discussed in the following sections.

Both the 4-h averaged f_oF_2 values using 1st and the Δf_oF_2 values using 2nd and 3rd show significant seasonal differences for both storm types when the occurring electron density ranges are considered. Winter and equinox storms generate electron density variability in a wider range, in contrast to the summer ones [64–66]. Additionally, in winter, the diurnal variation of the values varies over a wider range of 2–12 MHz for both ICME and SIR/CIR events, which also agrees with Zhang et al. [66]. Generally, during winter, we expect, in most cases, electron density to increase in response to geomagnetic disturbances during daylight hours at midlatitude [29,35,67,68]; this behavior is also reflected in our data analyzed with the first method. On the contrary, during summer, the occurrence of the negative ionospheric storm phase (both day and night) is most probable at midlatitude,

where Sopron station is located. Our data also confirms this expectation: the linear fitting on the different phases of the day groups of summer ICME and SIR/CIR events shows a decrease in foF2 as a function of the increasing geomagnetic indices in most of the cases. For winter events, only the Night and Midnight ICME-induced events show a positive foF2 trend as a function of geomagnetic indices. For the SIR/CIR-induced events, more than six events are needed to determine the trend. The various perturbations in the mid-latitude ionosphere during geomagnetic storms can be linked to different processes. The well-known drivers are the auroral heating of the thermosphere; seasonal variation of the background thermospheric wind circulation; O/N₂ ratio depletion, the increased temperature of the heated thermospheric gas; downwelling of the neutral atomic oxygen, and the uplifting of the F-layer along the magnetic field lines due to wind-induced vertical ExB drift; equatorward propagation of the main ionospheric trough, etc. [29,34,41,69–71]. More analysis is required if we want to determine the key drivers during these storm events.

As for the differences, in Figure 7 the deltafoF2 parameter of all storm events is portrayed, separated by only seasons. This shows the seasonal dependencies nicely: events triggered by SIR/CIR show a more significant seasonal dependency than those triggered by ICME. In Figures S1–S3, the groups according to the categorization by the local time of Dst_{min} show the same patterns. In conclusion, our investigation indicates that ICME-induced events cause electron density variability in a wider range, while SIR/CIR-caused perturbations show more predictable seasonal and Dst_{min} time dependencies.

However, if we take into account the daily and geomagnetic activity-related variations together (in the third method), the ICME-induced events do show significant seasonal and geomagnetic activity-dependent differences in Figures 8–10. Winter ICME-induced events and SIR/CIRs in Figure 8 for all three Dst_{min} groups show an increasing electron density trend as a function of increasing geomagnetic index. On the contrary, the post-midnight and phase-of-the-day groups of summer ICME-induced events show a significantly decreased tendency as a function of geomagnetic indices. These results also agree with the above-detailed seasonal dependence.

Interestingly, taking into account the time (UT), maximum peaks in deltafoF2 values (one or two peaks) are observed around noon and after 18:00 (most often around midnight) as geomagnetic activity increases. This behavior is observed in the data for both storm types. The double peak feature was observed in the daytime groups (Figure 8c,d) for winter ICME-induced events. The post-midnight, daytime, and pre-midnight data of the summer SIR/CIR group show an increasing electron density trend as a function of geomagnetic indices, with a double peak of deltafoF2 values in the morning and sunset sectors at the time of the geomagnetic index maxima (Figure 9b,d,f), like the previous case. These twin peaks with the midday bite out in the electron density at midlatitude have also been reported in the literature [72,73]. The summer pre-midnight group and the winter daytime ICME group show one peak in the deltafoF2, around noon or after sunset. Increased values after sunset (commonly referred to in the literature as the “dusk effect” [29,34,74] are also clearly visible in the results of second method for both storm types in winter (Figure 7), too. Several mechanisms have been suggested as potential causes of this phenomenon, such as uplifting of the ionosphere to regions where the recombination is low due to the enhanced neutral winds related to TADs or by electric fields ([75] and references therein).

Previous studies proposed the comparison of the foF2 parameter with the f10.7 solar flux index, sunspot number index (Rz) monthly mean, and Ly-alpha index, and they also used linear fitting on the data [76–78]. Danilov and Konstantinova [78] assumed that the f10.7 values do not correctly describe the solar ultraviolet variation in solar cycle 24. Therefore, the correction of this index is needed (they call it f10.7sm12) if one would like to get the true/reasonable foF2 trend, which was made by using the sunspot number index (Rz) and intensity of the Lyman- α line in the solar spectrum (Ly). When they used the corrected index instead of the regularly used f10.7 parameter, the correlation coefficient increased from ~0.5 up to 0.9. In our present study, the best correlation coefficient, $R = 0.81$, where

RMSD = 0.49, was found between the Dst index and the foF2 parameter by the Night group of summer ICME-induced events. Furthermore, the authors found a linearly decreasing trend in ΔfoF2 in time, correlated with the corrected f10.7 parameter. In our case, the linear fitting seemed to be the best between the Dst and foF2 with RMSD = 0.258 by the Midnight group of the winter SIR/CIR events. Another study by Ouattara and Zerbo [76] used the aa geomagnetic and the f10.7 solar activity indices to determine the correlation between the variation of the foF2 and h'F2 parameters and the indices during three solar cycle (20, 21, and 22). They conducted a similar investigation as we did in this paper but for the equatorial region. As a supplement to their work, we continued the correlation of the ionospheric foF2 parameter with other indices to find the best, which could be used as an indicator of ionospheric electron density changes during geomagnetic storms at midlatitude in the Northern Hemisphere. The geomagnetic Kp, Dst, and AE indices were used in this current study. During the comparison of the indices, we found that the most stable linear fitting in Figure 2, Figure 4, and Figure 6 was firstly for Dst indices, then for Kp. They found a very good correlation between the foF2 and F10.7 parameters (correlation coefficient 0.953), which means a much stronger correlation between the solar activity and the F2-layer electron density that can be determined by our results. Nevertheless, they analyzed the effect of severe shock and fluctuating activities (when aa \geq 100 nT) on the F2-layer, while in our case the impact of the less intense geomagnetic storms is also considered. Furthermore, we investigated the relationship between the foF2 and Dst, Kp, and AE indexes instead of the F10.7 parameter itself. These two factors can explain the large difference between the values of the correlation coefficients found by them and our study. Furthermore, the AE index indicated ionospheric disturbances might come with time delay to the latitude of Sopron station; therefore, this needs, e.g., cross-correlation analysis of AE index and foF2/ ΔfoF2 data to see the exact time delays between the source and the detected ionospheric perturbation above an individual ionosonde station.

In their article, Mendillo and Narvaez [1] concluded that the characteristic disturbance patterns are more likely to LT-dependent mechanisms: for positive phase—thermospheric wind, electric fields, and particle precipitation, while for negative phase—daytime O/N₂ changes and the nighttime drift of the midlatitude ionospheric trough. Therefore, we suggest the comparison of the ionospheric foF2 parameter with local or regional geomagnetic storm-related indices like the hourly range of absorption (HRA), which represents the localized features of ionospheric absorption at the auroral region, or the hourly range of the magnetic field (HR) [79]. It was stated in the previous article that the hourly range of the magnetic field seems to be a stronger indicator than Kp for characterizing auroral absorption [79]. Another suitable regional index for midlatitude can be the longitudinally asymmetric (ASY) and a symmetric (SYM) disturbance index with very high time resolution (1-min), which are introduced and derived for both H and D components [80,81]. The SYM-H index measures the intensity of the storm-time ring current [81–83]. The Ap (just like Kp) index quantifies the disturbance in the horizontal component of the Earth's magnetic field arising from the midlatitude ionospheric current system [84]. It can be interesting to correlate the foF2 data with the Hp30, Hp60, and ap30 indices, which are produced by Geomagnetic Observatory Niemegk, GFZ German Research Centre for Geosciences [85]. Both indices are unitless. Besides, the simultaneous investigation of dual-hemisphere stations during the same storm events can be also relevant as proposed by Mendillo and Narvaez [1], because it is important to get to know better the dependencies and differences between the two hemispheres if we want to predict the space weather effects with an empirical model in the future [48,49,52].

A new analysis concept of foF2 variability during geomagnetic storms arising from different sources (ICME or SIR/CIR) is proposed as a result of this study. The main conclusions are the following:

- During the investigation of the different phase of the day groups using 4-h average foF2 data (first method based on [23]), our main conclusion is, that winter ICME-driven events show a decreasing trend as a function of increasing geomagnetic indices at

Dawn, Morning and Noon group. On the contrary, an increasing trend is observed in Afternoon/Dusk and Night groups by ICME-driven events. For SIR/CIR-driven events, we cannot determine an obvious trend as a result of the few amount of events.

- In summer, a decrease in foF2 as a function of increasing geomagnetic activity is observed in most cases for both ICME- and SIR/CIR-driven events.
- Equinox events behave similarly to the summer ones, the difference is that the data points are more scattered, therefore the fitting is less reliable.
- Based on our results of the first analysis method, it is strengthened that more than six events are needed if we want to determine any trend in the foF2 parameter as a function of any geomagnetic index.
- The most significant correlations were between the Dst index and the foF2 parameter for the summer Night groups. The linear fitting is the most reliable based on the RMSD between the Dst and foF2 with $\text{RMSD} = 0.258$ for the winter SIR/CIR Midnight group.
- The trends of the linear fitting are fairly consistent with the literature on the behavior of the electron density in the F2 layer as a function of time during different seasons and phases of the day.
- The second method, ICME, can cause a larger disturbance in the F2 layer electron density both in the negative and positive directions, while the impact caused by the SIR/CIR-driven storms is more moderate and predictable.
- Representation of the data by the third method (3D plots), gives a better picture of the changes in electron density as a function of increasing geomagnetic activity and time.
- We conclude that ICME-induced events cause electron density changes over a wider range, while SIR/CIR-induced perturbations are more predictable.
- Another important conclusion is that if one would like to compare the ionospheric effects of the ICME and SIR/CIR-driven geomagnetic storms, the time of the Dst_{\min} can be used instead of the time of the SSC since generally there is no SSC for the SIR/CIR-driven storms. Nevertheless, the time of the Dst_{\min} should always be taken into account, as different ionospheric responses can be expected depending on the time of day when the Dst_{\min} occurred, thus when the ring current was the strongest.
- Our analysis strengthens the main seasonal dependence of the ionospheric response found by previous studies that the positive phase is more probable in winter, while the negative phase occurs mainly in summer in the Northern Hemisphere.
- We have also found by our analysis (second and third methods) some of the typical diurnal patterns of the foF2 during geomagnetic storms (previously described in the literature), such as the twin peaks with the midday bite or the “dusk effect” after sunset.
- In future studies, it will be important to investigate these events using other analysis methods, like, e.g., superposed epoch analysis, where we plan and suggest using local times of Dst_{\min} as the null time and longer time interval (36 h instead of 24). Furthermore, we find it important to use cross-correlation analysis on these data to disclose the time-shifted ionospheric changes caused by the geomagnetic storms. In addition, using more Digisonde station data (from Europe and the opposite hemisphere) and other local and regional geomagnetic/ionospheric indices is also an important aim in the next research project.

Supplementary Materials: The following supporting information can be downloaded at: <https://www.mdpi.com/article/10.3390/atmos14091377/s1>, Figure S1: The winter ICME versus SIR/CIR plots: (a,b) post-midnight, (c,d) daytime, (e,f) pre-midnight deltafoF2 (%) values in the function of time (UT). With colored dotted lines, the Dst_{\min} times are marked; Figure S2: The summer ICME versus SIR/CIR plots: (a,b) post-midnight, (c,d) daytime, (e,f) pre-midnight deltafoF2 (%) values in the function of time (UT). With colored dotted lines, the Dst_{\min} times are marked. Figure S3: The equinox ICME versus SIR/CIR plots: (a,b) post-midnight, (c,d) daytime, (e,f) pre-midnight deltafoF2 (%) values in the function of time (UT). With colored dotted lines, the Dst_{\min} times are marked; Table S1: Information about the clear ICME-related geomagnetic storm events from 2012–2014;

Table S2: Information about the clear SIR/CIR-related geomagnetic storm events from 2012–2014; Table S3: The reference Q-days for the analysis; Table S4: The linear fitting results with the root mean square deviation (RMSD) and the related correlation coefficient (R) values for ICME events' daytime groups with the values of the residuals; Table S5: The linear fitting results with the root mean square deviation (RMSD) and the related correlation coefficient (R) values for SIR/CIR events' daytime groups with the values of the residuals; Table S6: The 4-h mean values and their standard deviation for the SIR/CIR and ICME events. Each column represents the values of the different event day, in the order of Table S1 and S2, respectively; Table S7: The Dst minimum categorization of the events.

Author Contributions: K.A.B. was the main writer of the article, which contained the preparation of the event lists, figure making, and discussion of the results. V.B. actively contributed to the whole process; she helped during the analysis of the events and in the construction of the manuscript. A.O. and Z.D. checked the storm events using their great ability to recognize and list the ICME and SIR/CIR events coming from the Sun in satellite data. Á.K. gave ideas during the analysis of the events and Á.K. with A.O. reviewed some parts of the manuscript. Therefore, every author of this manuscript contributed substantially to this study. All authors have read and agreed to the published version of the manuscript.

Funding: The work of K.B. and V.B. was supported by the HORIZON 2020 T-FORS project (Grant Agreement No. 101081835). The contribution of V.B. was also supported by the Hungarian Scientific Research Fund grant no. PD141967 (OTKA) of the National Research, Development and Innovation Office (NKFIH) and through the Bolyai Fellowship no. BO/00461/21. The work of A.O. was funded by OTKA/NKFIH grant no. FK128548. Furthermore, this work was supported by the GINOP-2.3.2-15-2016-00003 project and a Hungarian funding no. SA-95/2021.

Institutional Review Board Statement: Not applicable.

Informed Consent Statement: Not applicable.

Data Availability Statement: The data used in this study was mostly publicly available. SC time were from: GFZ Potsdam, Germany: <https://www.gfz-potsdam.de/kp-index> and ISGI, Spain (International Service of Geo-magnetic Indices): http://isgi.unistra.fr/data_download.php. The ICME source dates were from these sites: <https://kauai.ccmc.gsfc.nasa.gov/CMEscoreboard/>; <https://izw1.caltech.edu/ACE/ASC/DATA/level3/icmetable2.htm>. The ACE/WIND collision dates available on <http://ipshocks.fi/database>, http://www.ssg.sr.unh.edu/mag/ace/ACELists/obs_list.html#2012 and <https://lweb.cfa.harvard.edu/shocks/> sites and also were determined by co-authors of this article: see Dalya & Opitz ACE ICME start and end dates [61]. The CIR, HSS catalogues, which were used for this analysis, available on <https://www.helcats-fp7.eu/> and <https://helioforecast.space/sircat> websites. Solar and geomagnetic indexes are from <https://omniweb.gsfc.nasa.gov/form/dx1.html> websites and the Dst-, AE- index and Dst_{min} times are from <http://wdc.kugi.kyoto-u.ac.jp/wdc/Sec3.html> site. For ionosonde data at Sopron station, see the following websites: <http://iono.nck.ggki.hu/ionogif/latest.html> and <http://reec.hu/iono.php> (all accessed on 20 August 2023).

Acknowledgments: The authors would like to thank the data to the Nagycenk Geophysical Observatory, Nagycenk, Hungary, which were the main basis of the research. The data service of OMNIWeb (<https://omniweb.gsfc.nasa.gov/form/dx1.html>, accessed on 20 August 2023) was crucial in the analysis of the geomagnetic indices. SSC data are partly from Observatori de l'Ebre (OE, Spain). Data of the observatories have been obtained from INTERMAGNET source. We thank the national institutes that support them and INTERMAGNET for promoting high standards of magnetic observatory practice (www.intermagnet.org). We acknowledge all the various experimenters who have made their data available through the ACE Science Center and other sources. Portions of that work were supported by a NASA Heliophysics Guest Investigator Grant and by the ACE mission.

Conflicts of Interest: The authors declare no conflict of interest.

References

- Mendillo, M.; Narvaez, C. Ionospheric storms at geophysically-equivalent sites—Part 2: Local time storm patterns for sub-auroral ionospheres. *Ann. Geophys.* **2010**, *28*, 1449–1462. [[CrossRef](#)]
- Gonzalez, W.D.; Joselyn, J.A.; Kamide, Y.; Kroehl, H.W.; Rostoker, G.; Tsurutani, B.T.; Vasyliunas, V.M. What is a geomagnetic storm? *J. Geophys. Res. Space Phys.* **1994**, *99*, 5771–5792. [[CrossRef](#)]
- Tsurutani, B.T.; Gonzalez, W.D.; Gonzalez, A.L.C.; Guarnieri, F.L.; Gopalswamy, N.; Grande, M.; Kamide, Y.; Kasahara, Y.; Lu, G.; Mann, I.; et al. Corotating solar wind streams and recurrent geomagnetic activity: A review. *J. Geophys. Res. Atmos.* **2006**, *111*, A07S01. [[CrossRef](#)]
- Denton, M.H.; Ulich, T.; Turunen, E. Modification of midlatitude ionospheric parameters in the F2 layer by persistent high-speed solar wind streams. *Space Weather* **2009**, *7*, 1–10. [[CrossRef](#)]
- Chen, G.-M.; Xu, J.; Wang, W.; Burns, A.G. A comparison of the effects of CIR- and CME-induced geomagnetic activity on thermospheric densities and spacecraft orbits: Statistical studies. *J. Geophys. Res. Space Phys.* **2014**, *119*, 7928–7939. [[CrossRef](#)]
- Chen, G.-M.; Xu, J.; Wang, W.; Lei, J.; Burns, A.G. A comparison of the effects of CIR- and CME-induced geomagnetic activity on thermospheric densities and spacecraft orbits: Case studies. *J. Geophys. Res. Atmos.* **2012**, *117*, 8315. [[CrossRef](#)]
- Shen, X.; Hudson, M.K.; Jaynes, A.N.; Shi, Q.; Tian, A.; Claudepierre, S.G.; Qin, M.; Zong, Q.; Sun, W. Statistical study of the storm time radiation belt evolution during Van Allen Probes era: CME- versus CIR-driven storms. *J. Geophys. Res. Space Phys.* **2017**, *122*, 8327–8339. [[CrossRef](#)]
- Crooker, N.U.; Cliver, E.W. Postmodern view of M-regions. *J. Geophys. Res. Atmos.* **1994**, *99*, 23383–23390. [[CrossRef](#)]
- Burns, A.G.; Solomon, S.C.; Wang, W.; Qian, L.; Zhang, Y.; Paxton, L.J. Daytime climatology of ionospheric N_mF_2 and h_mF_2 from COSMIC data. *J. Geophys. Res. Atmos.* **2012**, *117*, 9315. [[CrossRef](#)]
- Kamide, Y. Interplanetary and magnetospheric electric fields during geomagnetic storms: What is more important, steady-state fields or fluctuating fields? *J. Atmos. Sol. Terr. Phys.* **2001**, *63*, 413–420. [[CrossRef](#)]
- Buresova, D.; Lastovicka, J.; Hejda, P.; Bochnicek, J. Ionospheric disturbances under low solar activity conditions. *Adv. Space Res.* **2014**, *54*, 185–196. [[CrossRef](#)]
- Denton, M.H.; Borovsky, J.E.; Skoug, R.M.; Thomsen, M.F.; Lavraud, B.; Henderson, M.G.; McPherron, R.L.; Zhang, J.C.; Liemohn, M.W. Geomagnetic storms driven by ICME- and CIR-dominated solar wind. *J. Geophys. Res. Atmos.* **2006**, *111*, 7. [[CrossRef](#)]
- Allen, R.C.; Ho, G.C.; Jian, L.K.; Mason, G.M.; Vines, S.K.; Lario, D. Predictive Capabilities and Limitations of Stream Interaction Region Observations at Different Solar Longitudes. *Space Weather* **2020**, *18*, e2019SW002437. [[CrossRef](#)]
- Tsurutani, B.T.; Gonzalez, W.D.; Kamide, Y. Magnetic Storms. *Surv. Geophys.* **1997**, *18*, 363–383. [[CrossRef](#)]
- Richardson, I.G. Solar wind stream interaction regions throughout the heliosphere. *Living Rev. Sol. Phys.* **2018**, *15*, 1–95. [[CrossRef](#)]
- Chi, Y.; Shen, C.; Luo, B.; Wang, Y.; Xu, M. Geoeffectiveness of Stream Interaction Regions From 1995 to 2016. *Space Weather* **2018**, *16*, 1960–1971. [[CrossRef](#)]
- McGranaghan, R.; Knipp, D.J.; McPherron, R.L.; Hunt, L.A. Impact of equinoctial high-speed stream structures on thermospheric responses. *Space Weather* **2014**, *12*, 277–297. [[CrossRef](#)]
- Tsurutani, B.T.; Smith, E.J.; Pyle, K.R.; Simpson, J.A. Energetic protons accelerated at corotating shocks: Pioneer 10 and 11 observations from 1 to 6 AU. *J. Geophys. Res. Atmos.* **1982**, *87*, 7389–7404. [[CrossRef](#)]
- Zheng, Y.; Fok, M.-C.; Khazanov, G.V. A radiation belt-ring current forecasting model. *Space Weather* **2003**, *1*, 1013. [[CrossRef](#)]
- Turner, N.E.; Cramer, W.D.; Earles, S.K.; Emery, B.A. Geoefficiency and energy partitioning in CIR-driven and CME-driven storms. *J. Atmos. Sol. Terr. Phys.* **2009**, *71*, 1023–1031. [[CrossRef](#)]
- Emery, B.A.; Richardson, I.G.; Evans, D.S.; Rich, F.J. Solar wind structure sources and periodicities of auroral electron power over three solar cycles. *J. Atmos. Sol. Terr. Phys.* **2009**, *71*, 1157–1175. [[CrossRef](#)]
- Bingham, S.T.W.R. The Storm Time Response of the Inner Magnetosphere during Coronal Mass Ejection and Corotating Interaction Region Driven Storms. Ph.D. Thesis, University of New Hampshire, Durham, NH, USA, 2019.
- Mendillo, M.; Narvaez, C. Ionospheric storms at geophysically-equivalent sites—Part 1: Storm-time patterns for sub-auroral ionospheres. *Ann. Geophys.* **2009**, *27*, 1679–1694. [[CrossRef](#)]
- Gopalswamy, N. Solar connections of geoeffective magnetic structures. *J. Atmos. Sol. Terr. Phys.* **2008**, *70*, 2078–2100. [[CrossRef](#)]
- Kane, T.A.; Makarevich, R.A. HF radar observations of the F region ionospheric plasma response to Storm Sudden Commencements. *J. Geophys. Res. Atmos.* **2010**, *115*, 1–13. [[CrossRef](#)]
- Matzka, J.; Stolle, C.; Yamazaki, Y.; Bronkalla, O.; Morschhauser, A. The Geomagnetic Kp Index and Derived Indices of Geomagnetic Activity. *Space Weather* **2021**, *19*, e2020SW002641. [[CrossRef](#)]
- Campbell, W.H. Geomagnetic storms, the Dst ring-current myth and lognormal distributions. *J. Atmos. Terr. Phys.* **1996**, *58*, 1171–1187. [[CrossRef](#)]
- Daglis, I.A. Ring Current Dynamics. *Space Sci. Rev.* **2006**, *124*, 183–202. [[CrossRef](#)]
- Danilov, A. Ionospheric F-region response to geomagnetic disturbances. *Adv. Space Res.* **2013**, *52*, 343–366. [[CrossRef](#)]
- Burton, R.K.; McPherron, R.L.; Russell, C.T. An empirical relationship between interplanetary conditions and Dst. *J. Geophys. Res. Atmos.* **1975**, *80*, 4204–4214. [[CrossRef](#)]
- Kalegaev, V.V.; Makarenkov, E.V. Dynamics of magnetospheric current systems during magnetic storms of different intensity. *Geomagn. Aeron.* **2006**, *46*, 570–579. [[CrossRef](#)]

32. Rishbeth, H.; Field, P. Latitude and solar-cycle patterns in the response of the ionosphere F₂-layer to geomagnetic activity. *Adv. Space Res.* **1997**, *20*, 1689–1692. [[CrossRef](#)]
33. Pröls, G.W. *Physics of the Earth's Space Environment: An Introduction*; Springer: Berlin/Heidelberg, Germany, 2004. [[CrossRef](#)]
34. Buonsanto, M. Ionospheric Storms—A Review. *Space Sci. Rev.* **1999**, *88*, 563–601. [[CrossRef](#)]
35. Mendillo, M. Storms in the ionosphere: Patterns and processes for total electron content. *Rev. Geophys.* **2006**, *44*, 1–47. [[CrossRef](#)]
36. Kumar, E.A.; Kumar, S. Geomagnetic Storm Effect on F₂-Region Ionosphere during 2012 at Low- and Mid-Latitude-Latitude Stations in the Southern Hemisphere. *Atmosphere* **2022**, *13*, 480. [[CrossRef](#)]
37. Burešová, D.; Laštovička, J. Pre-storm enhancements of foF₂ above Europe. *Adv. Space Res.* **2007**, *39*, 1298–1303. [[CrossRef](#)]
38. Danilov, A.D.; Lastovicka, J. Effects of geomagnetic storms on the ionosphere and atmosphere. *Int. J. Geomagn. Aeron.* **2001**, *2*, 209–224.
39. Zhai, C.; Tang, S.; Peng, W.; Cheng, X.; Zheng, D. Driver of the Positive Ionospheric Storm over the South American Sector during 4 November 2021 Geomagnetic Storm. *Remote Sens.* **2023**, *15*, 111. [[CrossRef](#)]
40. Bojilova, R.; Mukhtarov, P. Response of the electron density profiles to geomagnetic disturbances in January 2005. *Stud. Geophys. Geod.* **2019**, *63*, 436–454. [[CrossRef](#)]
41. Berényi, K.A.; Heilig, B.; Urbář, J.; Kouba, D.; Kis, Á.; Barta, V. Comprehensive analysis of the ionospheric response to the largest geomagnetic storms from solar cycle 24 over Europe. *Front. Astron. Space Sci.* **2023**, *10*, 1092850. [[CrossRef](#)]
42. Immel, T.J.; Mannucci, A.J. Ionospheric redistribution during geomagnetic storms. *J. Geophys. Res. Space Phys.* **2013**, *118*, 7928–7939. [[CrossRef](#)]
43. Du, Z.L. The correlation between solar and geomagnetic activity—Part 1: Two-term decomposition of geomagnetic activity. *Ann. Geophys.* **2011**, *29*, 1331–1340. [[CrossRef](#)]
44. Du, Z.L. The correlation between solar and geomagnetic activity—Part 2: Long-term trends. *Ann. Geophys.* **2011**, *29*, 1341–1348. [[CrossRef](#)]
45. Brown, S.; Bilitza, D.; Yiğit, E. Ionosonde-based indices for improved representation of solar cycle variation in the International Reference Ionosphere model. *J. Atmos. Sol. Terr. Phys.* **2018**, *171*, 137–146. [[CrossRef](#)]
46. Gulyaeva, T.L.; Haralambous, H. Three-hourly Indices of Ionospheric Activity. *Geomagn. Aeron.* **2021**, *61*, 836–845. [[CrossRef](#)]
47. Gulyaeva, T.; Haralambous, H.; Stanislawski, I. Persistent perturbations of ionosphere at diminution of solar and geomagnetic activity during 21–24 solar cycles. *J. Atmos. Sol. Terr. Phys.* **2021**, *221*, 105706. [[CrossRef](#)]
48. Pietrella, M.; Perrone, L. A local ionospheric model for forecasting the critical frequency of the F₂ layer during disturbed geomagnetic and ionospheric conditions. *Ann. Geophys.* **2008**, *26*, 323–334. [[CrossRef](#)]
49. Perrone, L.; Mikhailov, A.V. SRF₂—A Short-Term (1–24)hf_oF₂ Prediction Method. *Space Weather* **2022**, *20*, e2022SW003047. [[CrossRef](#)]
50. Boroyev, R.N.; Vasiliev, M.S.; Baishev, D.G. The relationship between geomagnetic indices and the interplanetary medium parameters in magnetic storm main phases during CIR and ICME events. *J. Atmos. Sol. Terr. Phys.* **2020**, *204*, 105290. [[CrossRef](#)]
51. Mikhailov, A.V.; Perrone, L. Geomagnetic control of the midlatitude daytime f_oF₁ and f_oF₂ long-term variations: Physical interpretation using European observations. *J. Geophys. Res. Space Phys.* **2016**, *121*, 7193–7203. [[CrossRef](#)]
52. Tshisaphungo, M.; Habarulema, J.B.; McKinnell, L.-A. Modeling ionospheric foF₂ response during geomagnetic storms using neural network and linear regression techniques. *Adv. Space Res.* **2018**, *61*, 2891–2903. [[CrossRef](#)]
53. Zolesi, B.; Cander, L.R.; De Franceschi, G. Simplified ionospheric regional model for telecommunication applications. *Radio Sci.* **1993**, *28*, 603–612. [[CrossRef](#)]
54. Zolesi, B.; Cander, L.R.; De Franceschi, G. On the potential applicability of the simplified ionospheric regional model to different midlatitude areas. *Radio Sci.* **1996**, *31*, 547–552. [[CrossRef](#)]
55. Liu, L.; Wan, W.; Ning, B. Statistical modeling of ionospheric foF₂ over Wuhan. *Radio Sci.* **2004**, *39*, 1–10. [[CrossRef](#)]
56. Laštovička, J.; Mikhailov, A.; Ulich, T.; Bremer, J.; Elias, A.; de Adler, N.O.; Jara, V.; del Rio, R.A.; Foppiano, A.; Ovalle, E.; et al. Long-term trends in foF₂: A comparison of various methods. *J. Atmos. Sol. Terr. Phys.* **2006**, *68*, 1854–1870. [[CrossRef](#)]
57. Yue, X.; Wan, W.; Liu, L.; Ning, B.; Zhao, B. Applying artificial neural network to derive long-term foF₂ trends in the Asia/Pacific sector from ionosonde observations. *J. Geophys. Res. Atmos.* **2006**, *111*, 10303. [[CrossRef](#)]
58. Schmölter, E.; Berdermann, J. Predicting the Effects of Solar Storms on the Ionosphere Based on a Comparison of Real-Time Solar Wind Data with the Best-Fitting Historical Storm Event. *Atmosphere* **2021**, *12*, 1684. [[CrossRef](#)]
59. Berényi, K. Unique List of Clear ICME- and SIR/CIR-Related Geomagnetic Storm Events from the Maximum of 24 Solar Cycle (Nov 2012–Oct 2014). 2023. Volume 1. Available online: <https://data.mendeley.com/datasets/n245scjzk4/1> (accessed on 12 June 2023).
60. Dalya, Z.; Opitz, A.; Biro, N. Duration of ICME Signatures in In-Situ Data from Several Space Probes for the Time Interval of 2004–2021. 2023. Volume 1. Available online: <https://data.mendeley.com/datasets/4zwbp8k7cr/1> (accessed on 9 June 2023).
61. Bór, J.; Sători, G.; Barta, V.; Szabóné-André, K.; Szendrői, J.; Wsztergom, V.; Bozóki, T.; Buzás, A.; Koroncay, D. Measurements of atmospheric electricity in the Széchenyi István Geophysical Observatory, Hungary. *Hist. Geo Space Sci.* **2020**, *11*, 53–70. [[CrossRef](#)]
62. Berényi, K.; Barta, V.; Kis, Á. Midlatitude ionospheric F₂-layer response to eruptive solar events-caused geomagnetic disturbances over Hungary during the maximum of the solar cycle 24: A case study. *Adv. Space Res.* **2018**, *61*, 1230–1243. [[CrossRef](#)]
63. Barta, V.; Natras, R.; Srečković, V.; Koroncay, D.; Schmidt, M.; Šulic, D. Multi-instrumental investigation of the solar flares impact on the ionosphere on 05–06 December 2006. *Front. Environ. Sci.* **2022**, *10*, 1174. [[CrossRef](#)]
64. Rishbeth, H.; Mendillo, M. Patterns of F₂-layer variability. *J. Atmos. Sol. Terr. Phys.* **2001**, *63*, 1661–1680. [[CrossRef](#)]

65. Zou, L.; Rishbeth, H.; Müller-Wodarg, I.C.F.; Aylward, A.D.; Millward, G.H.; Fuller-Rowell, T.J.; Idenden, D.W.; Moffett, R.J. Annual and semiannual variations in the ionospheric F2-layer. I. Modelling. *Ann. Geophys.* **2000**, *18*, 927–944. [[CrossRef](#)]
66. Zhang, D.H.; Xiao, Z.; Hao, Y.-Q.; Ridley, A.J.; Moldwin, M. Modeling ionospheric foF2 by using empirical orthogonal function analysis. *Ann. Geophys.* **2011**, *29*, 1501–1515. [[CrossRef](#)]
67. Kil, H.; Paxton, L.J.; Pi, X.; Hairston, M.R.; Zhang, Y. Case study of the 15 July 2000 magnetic storm effects on the ionosphere-driver of the positive ionospheric storm in the winter hemisphere. *J. Geophys. Res. Atmos.* **2003**, *108*. [[CrossRef](#)]
68. Araujo-Pradere, E.A.; Fuller-Rowell, T.J.; Codrescu, M.V. STORM: An empirical storm-time ionospheric correction model 1. Model description. *Radio Sci.* **2002**, *37*, 1–12. [[CrossRef](#)]
69. Prölss, G.W. Ionospheric F-region storms. In *Handbook of Atmospheric Electrodynamics*; CRC Press: Boca Raton, FL, USA, 1995; Volume 2, pp. 195–248. Available online: <https://cir.nii.ac.jp/crid/1570291225295033472> (accessed on 2 November 2022).
70. Danilov, A. New results in studying foF2 trends. *J. Atmos. Sol. Terr. Phys.* **2017**, *163*, 103–113. [[CrossRef](#)]
71. Heilig, B.; Stolle, C.; Kervalishvili, G.; Rauberg, J.; Miyoshi, Y.; Tsuchiya, F.; Kumamoto, A.; Kasahara, Y.; Shoji, M.; Nakamura, S.; et al. Relation of the Plasmapause to the Midlatitude Ionospheric Trough, the Sub-Auroral Temperature Enhancement and the Distribution of Small-Scale Field Aligned Currents as Observed in the Magnetosphere by THEMIS, RBSP, and Arase, and in the Topside Ionosphere by Swarm. *J. Geophys. Res. Space Phys.* **2022**, *127*, e2021JA029646. [[CrossRef](#)]
72. Zhang, S.-R.; Oliver, W.L.; Fukao, S.; Otsuka, Y. A study of the forenoon ionospheric F₂ layer behavior over the middle and upper atmospheric radar. *J. Geophys. Res. Atmos.* **2000**, *105*, 15823–15833. [[CrossRef](#)]
73. Lynn, K.J.W.; Gardiner-Garden, R.S.; Heitmann, A. The spatial and temporal structure of twin peaks and midday bite out in foF2 (with associated height changes) in the Australian and South Pacific low midlatitude ionosphere. *J. Geophys. Res. Space Phys.* **2014**, *119*, 10294–10304. [[CrossRef](#)]
74. Mendillo, M.; Papagiannis, M.D.; Klobuchar, J.A. Average behavior of the midlatitude F-region parameters N_T , N_{max} , and τ during geomagnetic storms. *J. Geophys. Res. Atmos.* **1972**, *77*, 4891–4895. [[CrossRef](#)]
75. Gong, Y.; Zhou, Q.; Zhang, S.D.; Aponte, N.; Sulzer, M.; González, S.A. The F region and topside ionosphere response to a strong geomagnetic storm at Arecibo. *J. Geophys. Res. Space Phys.* **2013**, *118*, 5177–5183. [[CrossRef](#)]
76. Ouattara, F.; Zerbo, J.L. Ouagadougou station F2 layer parameters, yearly and seasonal variations during severe geomagnetic storms generated by coronal mass ejections (CMEs) and fluctuating wind streams. *Int. J. Phys. Sci.* **2011**, *6*, 4854–4860.
77. De Haro Barbás, B.F.; Elias, A.G. Effect of the Inclusion of Solar Cycle 24 in the Calculation of foF2 Long-Term Trend for Two Japanese Ionospheric Stations. *Pure Appl. Geophys.* **2020**, *177*, 1071–1078. [[CrossRef](#)]
78. Danilov, A.; Konstantinova, A. Trends in foF2 and the 24th solar activity cycle. *Adv. Space Res.* **2020**, *65*, 959–965. [[CrossRef](#)]
79. Fiori, R.A.D.; Trichtchenko, L.; Balch, C.; Spanswick, E.; Groleau, S. Characterizing Auroral-Zone Absorption Based on Global Kp and Regional Geomagnetic Hourly Range Indices. *Space Weather* **2020**, *18*, e2020SW002572. [[CrossRef](#)]
80. Mid-Latitude Geomagnetic Indices ‘ASY’ and ‘SYM’ for 200 (Provisional). Available online: <https://wdc.kugi.kyoto-u.ac.jp/aeasy/asy.pdf> (accessed on 25 August 2023).
81. Imtiaz, N.; Younas, W.; Khan, M. Response of the low- to mid-latitude ionosphere to the geomagnetic storm of September 2017. *Ann. Geophys.* **2020**, *38*, 359–372. [[CrossRef](#)]
82. Rostoker, G. Geomagnetic indices. *Rev. Geophys.* **1972**, *10*, 935–950. [[CrossRef](#)]
83. Wanliss, J.A.; Showalter, K.M. High-resolution global storm index: Dst versus SYM-H. *J. Geophys. Res. Atmos.* **2006**, *111*, 2202. [[CrossRef](#)]
84. Jian, L.K.; Russell, C.T.; Luhmann, J.G. Comparing Solar Minimum 23/24 with Historical Solar Wind Records at 1 AU. *Sol. Phys.* **2011**, *274*, 321–344. [[CrossRef](#)]
85. Yamazaki, Y.; Matzka, J.; Stolle, C.; Kervalishvili, G.; Rauberg, J.; Bronkalla, O.; Morschhauser, A.; Bruinsma, S.; Shprits, Y.Y.; Jackson, D.R. Geomagnetic Activity Index Hpo. *Geophys. Res. Lett.* **2022**, *49*, e2022GL098860. [[CrossRef](#)]

Disclaimer/Publisher’s Note: The statements, opinions and data contained in all publications are solely those of the individual author(s) and contributor(s) and not of MDPI and/or the editor(s). MDPI and/or the editor(s) disclaim responsibility for any injury to people or property resulting from any ideas, methods, instructions or products referred to in the content.